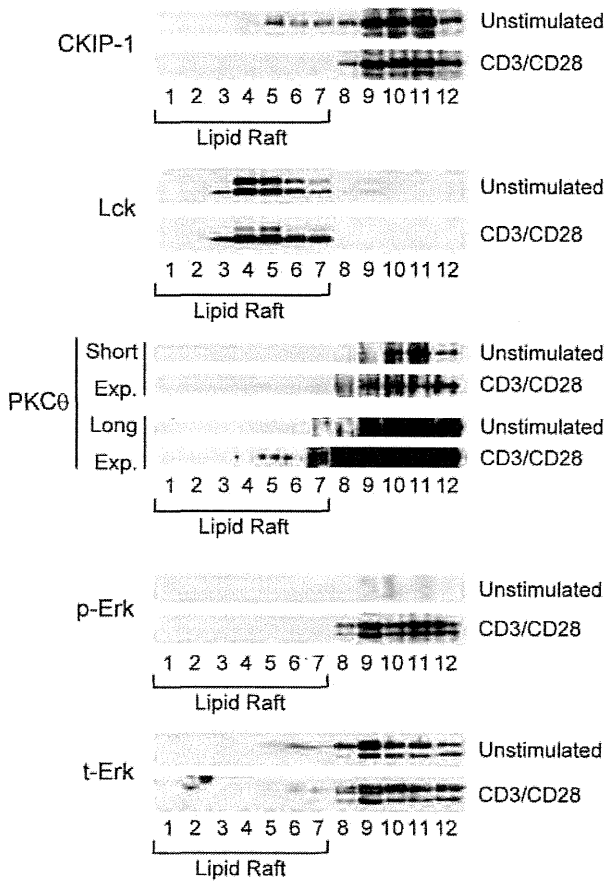

Figure 3. Lipid rafts accumulated by CD3/CD28 costimulation do not contain CKIP-1. Jurkat T cells were stimulated for 15 min with anti-CD3 (10 μg/ml) and anti-CD28 (5 μg/ml), together with 15 μg of mouse IgG. The cells were then lysed and subjected to OptiPrep density gradient centrifugation to isolate lipid rafts. Lysates were subjected to SDS-PAGE and analyzed by Western blotting.
doi:10.1371/journal.pone.0085762.g003

[28,35]. Phosphorylation of Erk was induced by CD3/CD28 costimulation. CKIP-1 partly localized at lipid rafts in unstimulated Jurkat T cells, and intriguingly, CKIP-1 was excluded from lipid rafts when cells were stimulated upon CD3/CD28 (Figure 3). These data suggest that, when cells are stimulated upon CD3/CD28 and lipid rafts are accumulated, CKIP-1 localizes out of the lipid rafts and its inhibitory effect does not extend.

Identification of CARMA1 as a binding partner of CKIP-1

To determine the interacting partner of CKIP-1, we examined whether CKIP-1 associates with PKCθ or CARMA1 by co-immunoprecipitation assays in HEK293T cells. CKIP-1 interacted with Myc-CARMA1 but not with PKCθ (Figure 4A, lane 1–4, Figure 4B, lane 1 and 2). In the presence of co-transfection of PKCθ, CKIP-1 also interacts with Myc-CARMA1 (Figure 4A, lane 5 and 6, Figure 4B, lane 3 and 4). We examined CKIP-1 and CARMA1 localization in HEK293T cells by confocal microscopy. HEK293T cells were transfected with DsRed-CKIP-1 and EGFP-CARMA1. The lipid rafts of transfected cells were stained with Alexa Flour 488-conjugated cholera toxin B (CTx). DsRed-CKIP-1 colocalized with Alexa Flour 488-CTx-labeled lipid rafts (Figure 4C, upper panel), and colocalized extensively with EGFP-CARMA1 (Figure 4C, lower panel). This result indicates that CKIP-1 colocalizes with CARMA1 at the plasma membrane.

Next, we examined the interaction between CKIP-1 and CARMA1 in T cells, using JPM50.6/WT cells, which were reconstituted with Myc-CARMA1 wild type (WT) in CARMA1-deficient Jurkat (JPM50.6) T cells [11,28]. Myc-CARMA1 was co-immunoprecipitated with endogenous CKIP-1 but not with control IgG (Figure 4D). To determine the domain of CARMA1 that was critical for the interaction with CKIP-1, truncated forms of CARMA1 were tested (Figure 4E). Co-immunoprecipitation assays showed that CKIP-1 bound to CARMA1 WT, CD-CC and ΔCD, but not to ΔCD-CC (Figure 4F), indicating that CKIP-1 associates with the CC domain of CARMA1. To determine the responsible region in CKIP-1 for the association with CARMA1, we generated several CKIP-1 truncated forms (Figure 4E). Co-immunoprecipitation assays revealed that CKIP-1 WT and ΔLZ bound to CARMA1 but CKIP-1 ΔPH did not (Figure 4G), indicating that the PH domain of CKIP-1 was essential for the interaction with CARMA1. To investigate direct interaction between CKIP-1 and CARMA1, *in vitro* GST pull-down assay was performed. GST-tagged CARMA1 CD-CC was able to interact with FLAG-CKIP-1 but GST was not (Figure 4H). Together, CARMA1 is a specific interacting partner of CKIP-1.

PH domain of CKIP-1 is essential for the interaction with CARMA1 and the inhibitory effect on NF-κB activation

Next we examined the function of each truncated form of CKIP-1 on NF-κB activation, using luciferase reporter assays. Jurkat T cells were transfected with each CKIP-1 truncated form and stimulated by PMA and CD3/CD28. CKIP-1 WT and ΔLZ inhibited NF-κB activation induced by stimulation with PMA, but CKIP-1 ΔPH did not (Figure 5A, middle panel). Similarly to CKIP-1 WT (Figure 1C), the truncated forms of CKIP-1 gave no influence upon CD3/CD28-induced-NF-κB activation (Figure 5A, right panel). In resting state, the effect of the truncated forms was not statistically significant, because of the little amount of NF-κB activity in unstimulated cells (Figure 5A, left panel). Jurkat T cells were transfected with PKCθ AE together with each CKIP-1 truncated form. CKIP-1 WT and ΔLZ suppressed NF-κB activation, but CKIP-1 ΔPH did not (Figure 5B, left panel). As shown in Figure 2A, NF-κB activation induced by CARMA1 seemed to be suppressed by CKIP-1 WT, but the effect was not statistically significant. Neither CKIP-1 ΔLZ nor ΔPH repressed NF-κB activation induced by CARMA1 (Figure 5B, right panel). These results suggest that PH domain of CKIP-1, which is required for association with CARMA1, is essential for the inhibitory effect on NF-κB activation.

CKIP-1 inhibits the interaction between PKCθ and CARMA1

PKCθ phosphorylates CARMA1 in its Linker between the CD-CC domain and the MAGUK domain, which induces conformational change of CARMA1 [7,8]. Then CARMA1 binds to Bcl10 through CARD-CARD interaction [9,36]. Since our data suggested that CKIP-1 interacted with the CC domain of CARMA1, we hypothesized that CKIP-1 might inhibit the interaction between CARMA1 and PKCθ or between CARMA1 and Bcl10. Co-immunoprecipitation assays showed that CKIP-1 inhibited the interaction between PKCθ and CARMA1, but not that between CARMA1 and Bcl10 (Figure 6A). As shown in Figure 4B (lane 5 and 6), PKCθ was immunoprecipitated with Myc-CARMA1, but, in the presence of co-transfection of CKIP-1, the interaction between PKCθ and CARMA1 was diminished (Figure 4B, lane 3 and 4). Next, we examined the inhibitory effect of CKIP-1 truncated forms on the interaction between PKCθ and

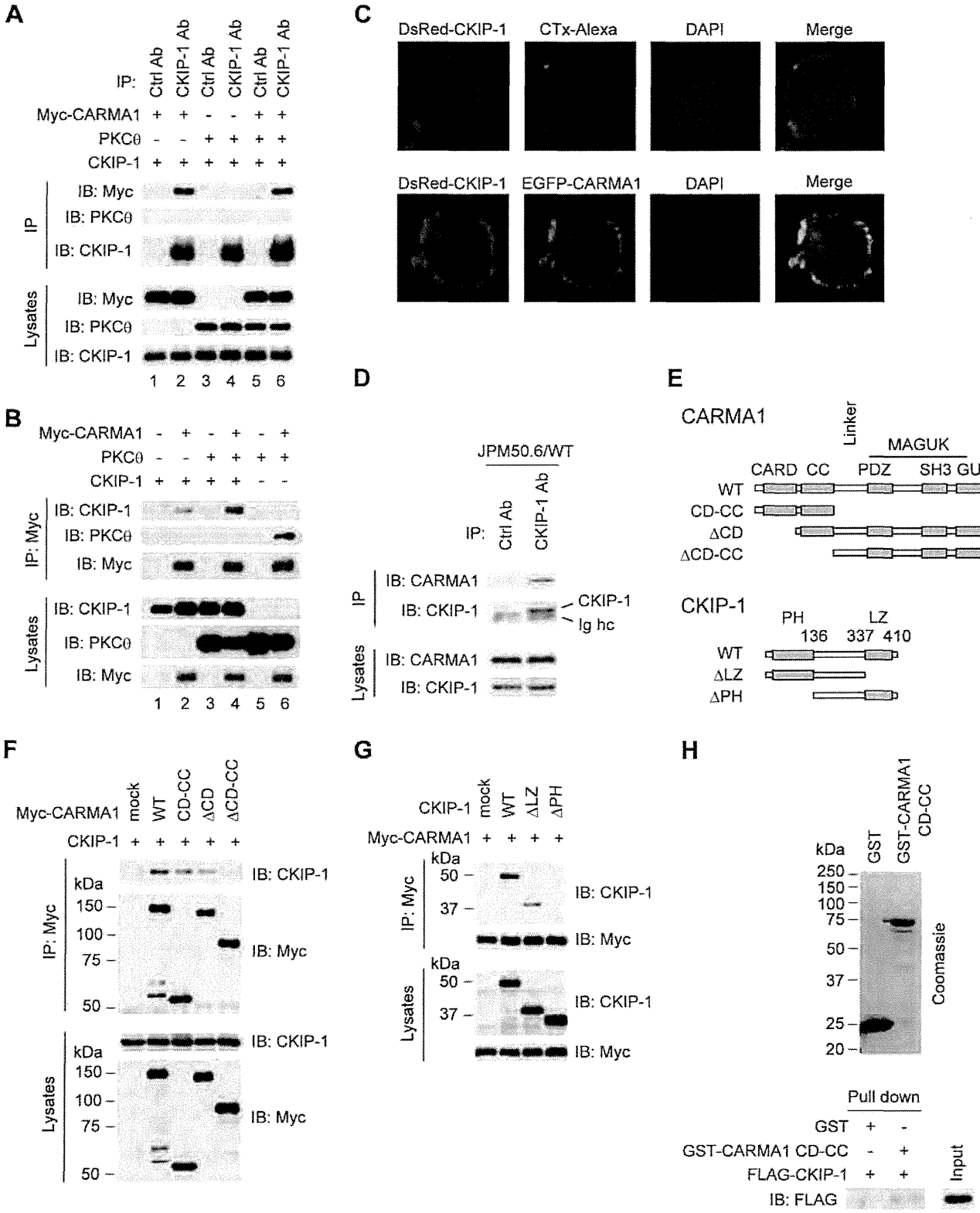

Figure 4. Identification of CARMA1 as a binding partner of CKIP-1. (A) HEK293T cells were transfected with plasmids encoding CKIP-1 together with Myc-CARMA1 or PKCθ, lysed, and immunoprecipitated by anti-CKIP-1 or control antibody. (B) HEK293T cells were co-transfected with plasmids encoding Myc-CARMA1, PKCθ or CKIP-1, lysed, and immunoprecipitated by anti-Myc antibodies. (C) HEK293T cells were transfected with DsRed-CKIP-1. 24 hr later, the transfected cells were incubated with Alexa Flour 488-conjugated cholera toxin B (CTx), and were fixed and stained with DAPI. In lower panels, HEK293T cells were transfected with DsRed-CKIP-1 together with EGFP-CARMA1. 24 hr later, cells were fixed and stained with DAPI. The localization of CKIP-1, CARMA1 and Alexa Flour 488-CTx-labeled lipid rafts was visualized by confocal microscopy. (D) JPM50.6/WT cells, which were reconstituted by Myc-CARMA1 WT into CARMA1-deficient Jurkat T cells, were lysed and immunoprecipitated by anti-CKIP-1 or control antibody. Ig hc, immunoglobulin heavy chain. (E) Schematic diagram of CARMA1 and CKIP-1 truncated forms used in the experiments. CARD,

caspase recruitment domain; CC, coiled-coil; SH3, Src homology 3; GUK, guanylate kinase; MAGUK, membrane-associated GUK; PH, pleckstrin homology; LZ, leucin zipper. (F) HEK293T cells were transfected with CKIP-1 together with Myc-CARMA1 truncated form, lysed, and immunoprecipitated by anti-Myc antibody, followed by Western blotting with indicated antibodies. (G) HEK293T cells were transfected with Myc-CARMA1 together with each CKIP-1 truncated form. Cell lysates were immunoprecipitated by anti-Myc antibody, followed by Western blotting with indicated antibodies. (H) CARMA1 CD-CC was purified from *E. coli* as a GST fusion protein. GST alone or GST-tagged CARMA1 CD-CC was incubated with *in vitro* transcribed/translated FLAG-CKIP-1. GST pull-downs and input were subjected to Western blotting with anti-FLAG antibody.
doi:10.1371/journal.pone.0085762.g004

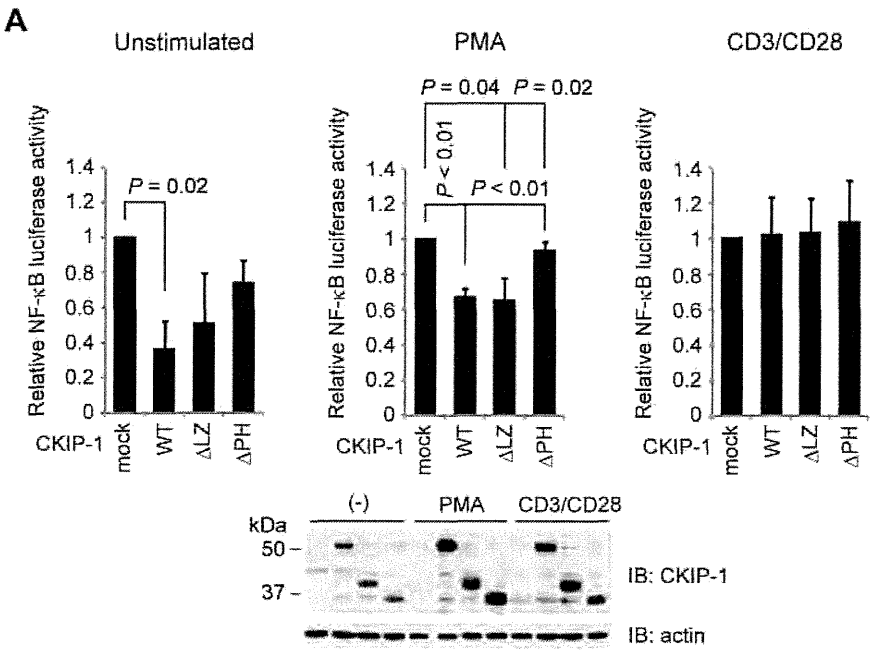

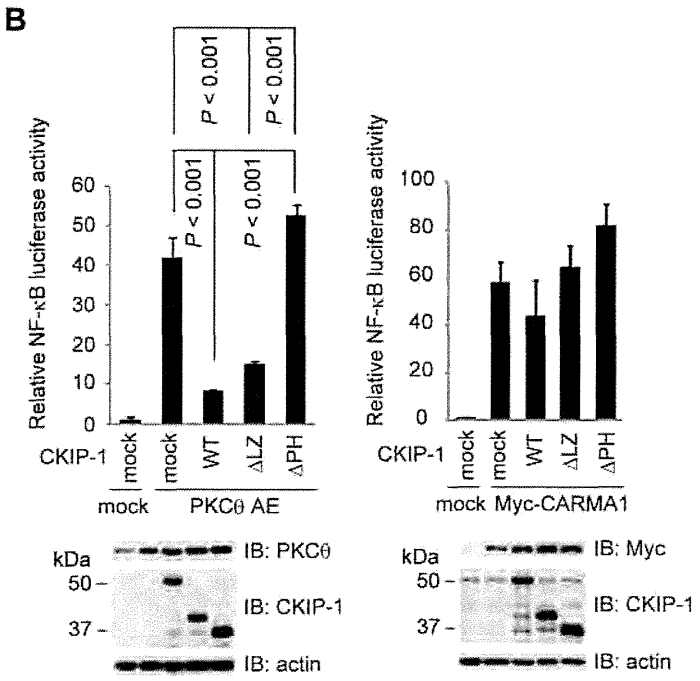

Figure 5. PH domain of CKIP-1 is essential not only for the interaction with CARMA1 but also for the inhibitory effect on NF-κB activation. (A) Jurkat T cells were electroporated with 5 μg of each CKIP-1 truncated form together with 5 μg of κB-Luc and 0.1 μg of *Renilla*-Luc. Nineteen hours later, cells were stimulated for 5 hr upon PMA (10 ng/ml) or CD3/CD28 (2 μg/ml each). The expressed protein levels were analyzed by Western blotting. (B) Jurkat T cells were electroporated with 5 μg of each CKIP-1 truncated form together with 5 μg of PKCθ AE or Myc-CARMA1, 5 μg of κB-Luc and 0.1 μg of *Renilla*-Luc. After 24 hr, cells were lysed and luciferase activity was assessed. The expressed protein levels were analyzed by Western blotting. Values represent the average of three independent experiments and error bars represent the SD from the average.
doi:10.1371/journal.pone.0085762.g005

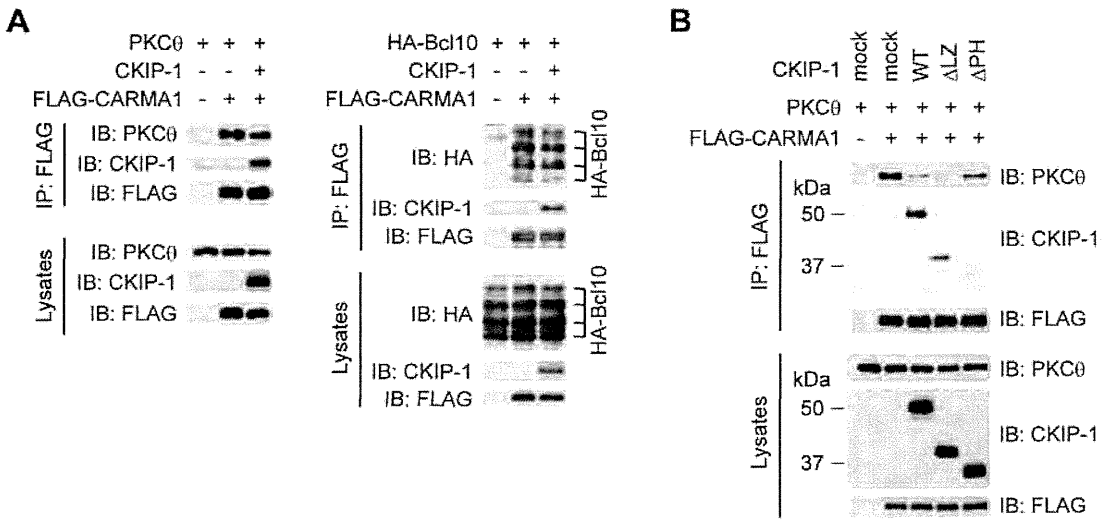

Figure 6. CKIP-1 inhibits the interaction between PKCθ and CARMA1. (A) HEK293T cells were transfected with CKIP-1 or empty vector (mock) together with PKCθ and FLAG-CARMA1 (left panel), or together with HA-Bcl10 and FLAG-CARMA1 (right panel). Cell lysates were immunoprecipitated by anti-FLAG antibody, followed by Western blotting with indicated antibodies. (B) HEK293T cells were transfected with CKIP-1 truncated form together with PKCθ and FLAG-CARMA1. Cell lysates were immunoprecipitated by anti-FLAG antibody, followed by Western blotting with indicated antibodies.
doi:10.1371/journal.pone.0085762.g006

CARMA1. Consistent with the results of the binding and the inhibitory effect of the truncated forms (Figure 4G and Figure 5), CKIP-1 WT and ΔLZ inhibited the interaction between PKCθ and CARMA1, although CKIP-1 ΔPH showed no effect (Figure 6B). These results suggest that CKIP-1 suppresses NF-κB activation by inhibiting the interaction between PKCθ and CARMA1.

Discussion

NF-κB signaling in antigen-stimulated lymphocytes plays an important role in immune response. Aberrant NF-κB activation has been shown to be involved in autoimmune diseases and malignant lymphomas. Especially, altered expression and/or function of CBM proteins have been reported in the ABC subtype of DLBCL [16,37,38] and MALT lymphoma [39].

In this study, we show that CKIP-1 is a novel interacting protein with CARMA1 and acts as a suppressor of NF-κB signaling. Our results suggest that CKIP-1 suppresses NF-κB signaling by inhibiting the interaction between PKCθ and CARMA1. However, CKIP-1 does not suppress NF-κB activation induced by CD3/CD28 costimulation. Our data suggest that it is because CKIP-1 localizes outside of the lipid rafts and its inhibitory effect does not extend, when cells are stimulated upon CD3/CD28 and lipid rafts are accumulated. A transmembrane adaptor molecule PAG/Cbp is also a negative regulator of T cell activation. In resting T cells, PAG/Cbp is phosphorylated by Lck and interacts with C-terminal Src kinase (Csk), which inhibits T cell activation by suppressing c-Src. In response to stimulation of TCR, PAG/Cbp becomes rapidly dephosphorylated and dissociates from Csk [40,41]. Likewise, IκBs usually retain NF-κB in the cytoplasm through physical interaction. In response to signaling, IκBs are phosphorylated, leading to their ubiquitylation and subsequent proteasomal degradation [42]. Similarly to PAG/Cbp or IκBs, CKIP-1 usually interacts with CARMA1, but its inhibitory effect might be abrogated during CD3/CD28 costimulation. We presume that CKIP-1 physiologically prevents T cells from being activated by inadequate stimulation and might play a role like a gatekeeper for correct CD3/CD28 signaling at the step of CARMA1 during antigen-stimulation. We speculate that, in resting T cells, CKIP-1 associates with CARMA1 and keeps PKCθ away from CARMA1. Our date clearly showed that when T cells are stimulated appropriately upon CD3/CD28 costimulation, both PKCθ and CARMA1 are recruited to lipid rafts. However, CKIP-1 remains outside of the lipid rafts, and its inhibitory effect cannot extend. CARMA1 is then phosphorylated by PKCθ at the lipid rafts leading to its conformational change into an active form. The activated CARMA1 recruits Bcl10-MALT1 complex and subsequently induces NF-κB activation.

PAG/Cbp-deficient mice exhibit no overt phenotype [43,44], but, in cancer cells, PAG/Cbp is involved in repressing the oncogenecity of c-Src [45]. CKIP-1-deficient mice are reported to undergo an age-dependent increase in bone mass [25]. However, no phenotype about immune disorders or neoplasm has been described. Thus, PAG/Cbp and CKIP-1 might be dispensable or could be compensated by some other negative regulators, because multiple checkpoints through TCR-mediated NF-κB signaling are likely to be independently required to prevent the unwarranted expansion and transformation of lymphocytes, and to ensure an appropriate adaptive immune response. Our data suggest that the suppression of CKIP-1 can work in a resting state or against aberrant PKCθ activation such as expression of constitutively active PKCθ or treatment of PMA. Similarly to PAG/Cbp, only in malignant lymphomas or immunological disorders, CKIP-1 might play a critical role as a suppressor of aberrant NF-κB activation.

Recently, novel germline CARMA1 mutations have been reported in four patients with congenital B cell lymphocytosis [17]. These CARMA1 mutants constitutively drive NF-κB activation, resulting in elevated NF-κB activity and increased proliferation of patient primary B cells. However, patient primary T cells expressing these CARMA1 mutants are hyporesponsive to CD3/CD28 costimulation. It has also been reported that chronic NF-κB activation, triggered by transgenic expression of constitutively active IKKβ in mice, renders T cells hyporesponsive to TCR stimulation [46]. We speculate that T cells have the mechanism by which an anergic state is induced by chronic active

NF-κB signaling, and it might be one of the reasons why knockdown of CKIP-1 did not exhibit clear phenotypes in TCR stimulation. Analysis of B cells might be useful for deciphering the physiological role of CKIP-1.

There have been already reported two inhibitory regulators that interact with CARMA1. The kinesin GAKIN negatively regulates occupancy of CARMA1 at the center of the immunological synapse, and limits the extent of signaling [47]. Casein kinase 1α (CK1α), which is reported to be a bifunctional regulator, also interacts with CARMA1 and terminates signaling by phosphorylating CARMA1 [48]. Although CKIP-1 interacts with CARMA1 as GAKIN and CK1α do, CKIP-1 shows several different aspects. Whereas GAKIN competes with Bcl10 for binding, CKIP-1 competes with PKCθ but not with Bcl10. GAKIN and CK1α associate with CARMA1 in a signal-dependent manner. On the other hand, CKIP-1 neither localizes at lipid rafts nor influences NF-κB activation during CD3/CD28 costimulation. To our knowledge, CKIP-1 is the first molecule that negatively regulates CARMA1 in a resting state or in aberrantly activated signaling.

In conclusion, we have herein demonstrated an inhibitory effect of CKIP-1 in PKCθ-CBM-NF-κB signaling. CKIP-1 interacts with CARMA1 and competes with PKCθ for binding. It suggests that CKIP-1 plays a unique role to keep resting T cells in a quiescent state or to prevent T cells from being activated by inadequate signaling. Dysfunction of CKIP-1 might constitutively activate NF-κB, leading to autoimmune diseases or malignant lymphomas, and the signaling events around CKIP-1 might be good therapeutic targets.

Supporting Information

Figure S1 Knockdown of CKIP-1 induces NF-κB activation. The JR-GFP cells were electroporated with 400 pmol of non-targeting siRNA, or specific siRNA against each gene by AMAXA Nucleofector System. Five days later, the expression of EGFP was assessed by FACS.
(TIF)

Acknowledgments

We thank Drs. T. Kitawaki and H. Fujita (University of Kyoto) for the manipulation of FACSAria cell sorter; Drs. T. Yoshida and T. Kobayashi (University of Kyoto) for the preparation of a human leukocyte-cDNA library; C. Sakamoto (University of Kyoto) for technical support.

Author Contributions

Conceived and designed the experiments: TS MK KT ATK. Performed the experiments: TS MK KN FI YT YA. Analyzed the data: KT MS KI KY KS NK. Contributed reagents/materials/analysis tools: KY YK. Wrote the paper: TS MK KS NK YK ATK.

References

1. Vallabhapurapu S, Karin M (2009) Regulation and function of NF-kappaB transcription factors in the immune system. Annu Rev Immunol 27: 693–733.
2. Kane LP, Lin J, Weiss A (2002) It's all Rel-ative: NF-kappaB and CD28 costimulation of T-cell activation. Trends Immunol 23: 413–420.
3. Dustin ML, Olszowy MW, Holdorf AD, Li J, Bromley S, et al. (1998) A novel adaptor protein orchestrates receptor patterning and cytoskeletal polarity in T-cell contacts. Cell 94: 667–677.
4. Dustin ML (2008) T-cell activation through immunological synapses and kinapses. Immunol Rev 221: 77–89.
5. Chuang HC, Lan JL, Chen DY, Yang CY, Chen YM, et al. (2011) The kinase GLK controls autoimmunity and NF-kappaB signaling by activating the kinase PKC-theta in T cells. Nat Immunol 12: 1113–1118.
6. Kong KF, Yokosuka T, Canonigo-Balancio AJ, Isakov N, Saito T, et al. (2011) A motif in the V3 domain of the kinase PKC-theta determines its localization in the immunological synapse and functions in T cells via association with CD28. Nat Immunol 12: 1105–1112.
7. Matsumoto R, Wang D, Blonska M, Li H, Kobayashi M, et al. (2005) Phosphorylation of CARMA1 plays a critical role in T Cell receptor-mediated NF-kappaB activation. Immunity 23: 575–585.
8. Sommer K, Guo B, Pomerantz JL, Bandaranayake AD, Moreno-Garcia ME, et al. (2005) Phosphorylation of the CARMA1 linker controls NF-kappaB activation. Immunity 23: 561–574.
9. Thome M, Charton JE, Pelzer C, Hailfinger S (2010) Antigen receptor signaling to NF-kappaB via CARMA1, BCL10, and MALT1. Cold Spring Harb Perspect Biol 2: a003004.
10. Blonska M, Lin X (2011) NF-kappaB signaling pathways regulated by CARMA family of scaffold proteins. Cell Res 21: 55–70.
11. Wang D, You Y, Case SM, McAllister-Lucas LM, Wang L, et al. (2002) A requirement for CARMA1 in TCR-induced NF-kappa B activation. Nat Immunol 3: 830–835.
12. Egawa T, Albrecht B, Favier B, Sunshine MJ, Mirchandani K, et al. (2003) Requirement for CARMA1 in antigen receptor-induced NF-kappa B activation and lymphocyte proliferation. Curr Biol 13: 1252–1258.
13. Hara H, Wada T, Bakal C, Kozieradzki I, Suzuki S, et al. (2003) The MAGUK family protein CARD11 is essential for lymphocyte activation. Immunity 18: 763–775.
14. Jun JE, Wilson LE, Vinuesa CG, Lesage S, Blery M, et al. (2003) Identifying the MAGUK protein Carma-1 as a central regulator of humoral immune responses and atopy by genome-wide mouse mutagenesis. Immunity 18: 751–762.
15. Newton K, Dixit VM (2003) Mice lacking the CARD of CARMA1 exhibit defective B lymphocyte development and impaired proliferation of their B and T lymphocytes. Curr Biol 13: 1247–1251.
16. Shaffer AL 3rd, Young RM, Staudt LM (2012) Pathogenesis of human B cell lymphomas. Annu Rev Immunol 30: 565–610.
17. Snow AL, Xiao W, Stinson JR, Lu W, Chaigne-Delalande B, et al. (2012) Congenital B cell lymphocytosis explained by novel germline CARD11 mutations. J Exp Med 209: 2247–2261.
18. Bosc DG, Graham KC, Saulnier RB, Zhang C, Prober D, et al. (2000) Identification and characterization of CKIP-1, a novel pleckstrin homology domain-containing protein that interacts with protein kinase CK2. J Biol Chem 275: 14295–14306.
19. Nie J, Liu L, He F, Fu X, Han W, et al. (2013) CKIP-1: a scaffold protein and potential therapeutic target integrating multiple signaling pathways and physiological functions. Ageing Res Rev 12: 276–281.
20. Safi A, Vandromme M, Caussanel S, Valdacci L, Baas D, et al. (2004) Role for the Pleckstrin Homology Domain-Containing Protein CKIP-1 in Phosphatidylinositol 3-Kinase-Regulated Muscle Differentiation. Mol Cell Biol 24: 1245–1255.
21. Canton DA, Olsten ME, Kim K, Doherty-Kirby A, Lajoie G, et al. (2005) The pleckstrin homology domain-containing protein CKIP-1 is involved in regulation of cell morphology and the actin cytoskeleton and interaction with actin capping protein. Mol Cell Biol 25: 3519–3534.
22. Zhang L, Xing G, Tie Y, Tang Y, Tian C, et al. (2005) Role for the pleckstrin homology domain-containing protein CKIP-1 in AP-1 regulation and apoptosis. EMBO J 24: 766–778.
23. Zhang L, Tie Y, Tian C, Xing G, Song Y, et al. (2006) CKIP-1 recruits nuclear ATM partially to the plasma membrane through interaction with ATM. Cell Signal 18: 1386–1395.
24. Tokuda E, Fujita N, Oh-hara T, Sato S, Kurata A, et al. (2007) Casein kinase 2-interacting protein-1, a novel Akt pleckstrin homology domain-interacting protein, down-regulates PI3K/Akt signaling and suppresses tumor growth in vivo. Cancer Res 67: 9666–9676.
25. Lu K, Yin X, Weng T, Xi S, Li L, et al. (2008) Targeting WW domains linker of HECT-type ubiquitin ligase Smurf1 for activation by CKIP-1. Nat Cell Biol 10: 994–1002.
26. Ling S, Sun Q, Li Y, Zhang L, Zhang P, et al. (2012) CKIP-1 Inhibits Cardiac Hypertrophy by Regulating Class II Histone Deacetylase Phosphorylation through Recruiting PP2A. Circulation.
27. Wang Y, Nie J, Zhang L, Lu K, Xing G, et al. (2012) CKIP-1 couples Smurf1 ubiquitin ligase with Rpt6 subunit of proteasome to promote substrate degradation. EMBO Rep 13: 1004–1011.
28. Wang D, Matsumoto R, You Y, Che T, Lin XY, et al. (2004) CD3/CD28 costimulation-induced NF-kappaB activation is mediated by recruitment of protein kinase C-theta, Bcl10, and IkappaB kinase beta to the immunological synapse through CARMA1. Mol Cell Biol 24: 164–171.
29. Cvijic ME, Xiao G, Sun SC (2003) Study of T-cell signaling by somatic cell mutagenesis and complementation cloning. Journal of Immunological Methods 278: 293–304.
30. Kawano Y, Yoshida T, Hieda K, Aoki J, Miyoshi H, et al. (2004) A lentiviral cDNA library employing lambda recombination used to clone an inhibitor of

human immunodeficiency virus type 1-induced cell death. J Virol 78: 11352–11359.
31. Yoshida T, Kawano Y, Sato K, Ando Y, Aoki J, et al. (2008) A CD63 Mutant Inhibits T-cell Tropic Human Immunodeficiency Virus Type 1 Entry by Disrupting CXCR4 Trafficking to the Plasma Membrane. Traffic 9: 540–558.
32. Baier-Bitterlich G, Uberall F, Bauer B, Fresser F, Wachter H, et al. (1996) Protein kinase C-theta isoenzyme selective stimulation of the transcription factor complex AP-1 in T lymphocytes. Mol Cell Biol 16: 1842–1850.
33. Wertz IE, O'Rourke KM, Zhou H, Eby M, Aravind L, et al. (2004) De-ubiquitination and ubiquitin ligase domains of A20 downregulate NF-kappaB signalling. Nature 430: 694–699.
34. Gaide O, Favier B, Legler DF, Bonnet D, Brissoni B, et al. (2002) CARMA1 is a critical lipid raft-associated regulator of TCR-induced NF-kappa B activation. Nat Immunol 3: 836–843.
35. Bromley SK, Burack WR, Johnson KG, Somersalo K, Sims TN, et al. (2001) The immunological synapse. Annu Rev Immunol 19: 375–396.
36. Blonska M, Lin X (2009) CARMA1-mediated NF-kappaB and JNK activation in lymphocytes. Immunol Rev 228: 199–211.
37. Lenz G, Davis RE, Ngo VN, Lam L, George TC, et al. (2008) Oncogenic CARD11 mutations in human diffuse large B cell lymphoma. Science 319: 1676–1679.
38. Ngo VN, Davis RE, Lamy L, Yu X, Zhao H, et al. (2006) A loss-of-function RNA interference screen for molecular targets in cancer. Nature 441: 106–110.
39. Lim KH, Yang Y, Staudt LM (2012) Pathogenetic importance and therapeutic implications of NF-kappaB in lymphoid malignancies. Immunol Rev 246: 359–378.
40. Brdicka T, Pavlistova D, Leo A, Bruyns E, Korinek V, et al. (2000) Phosphoprotein associated with glycosphingolipid-enriched microdomains (PAG), a novel ubiquitously expressed transmembrane adaptor protein, binds the protein tyrosine kinase csk and is involved in regulation of T cell activation. J Exp Med 191: 1591–1604.
41. Davidson D, Bakinowski M, Thomas ML, Horejsi V, Veillette A (2003) Phosphorylation-dependent regulation of T-cell activation by PAG/Cbp, a lipid raft-associated transmembrane adaptor. Mol Cell Biol 23: 2017–2028.
42. Hayden MS, Ghosh S (2008) Shared principles in NF-kappaB signaling. Cell 132: 344–362.
43. Dobenecker MW, Schmedt C, Okada M, Tarakhovsky A (2005) The ubiquitously expressed Csk adaptor protein Cbp is dispensable for embryogenesis and T-cell development and function. Mol Cell Biol 25: 10533–10542.
44. Xu S, Huo J, Tan JE, Lam KP (2005) Cbp deficiency alters Csk localization in lipid rafts but does not affect T-cell development. Mol Cell Biol 25: 8486–8495.
45. Oneyama C, Hikita T, Enya K, Dobenecker MW, Saito K, et al. (2008) The lipid raft-anchored adaptor protein Cbp controls the oncogenic potential of c-Src. Mol Cell 30: 426–436.
46. Krishna S, Xie D, Gorentla B, Shin J, Gao J, et al. (2012) Chronic activation of the kinase IKKbeta impairs T cell function and survival. J Immunol 189: 1209–1219.
47. Lamason RL, Kupfer A, Pomerantz JL (2010) The dynamic distribution of CARD11 at the immunological synapse is regulated by the inhibitory kinesin GAKIN. Mol Cell 40: 798–809.
48. Bidere N, Ngo VN, Lee J, Collins C, Zheng L, et al. (2009) Casein kinase 1alpha governs antigen-receptor-induced NF-kappaB activation and human lymphoma cell survival. Nature 458: 92–96.

VIP Real-Time NMR Spectroscopy Very Important Paper

DOI: 10.1002/anie.201309940

Quantitative Analysis of Location- and Sequence-Dependent Deamination by APOBEC3G Using Real-Time NMR Spectroscopy**

*Ayako Furukawa, Kenji Sugase, Ryo Morishita, Takashi Nagata, Tsutomu Kodaki, Akifumi Takaori-Kondo, Akihide Ryo, and Masato Katahira**

Abstract: *The human antiretroviral factor APOBEC3G (A3G) deaminates the newly synthesized minus strand of the human immunodeficiency virus 1 (HIV-1), which results in the abolition of the infectivity of virus-infectivity-factor (Vif)-deficient HIV-1 strains.[1–6] A unique property of A3G is that it deaminates a CCC hot spot that is located close to the 5′ end more effectively than one that is less close to the 5′ end. However, the mechanism of this process is elusive as it includes nonspecific binding of A3G to DNA and sliding of A3G along the DNA strand. Therefore, this process cannot be analyzed by existing methods using the Michaelis–Menten theory. A new real-time NMR method has been developed to examine the nonspecific binding and the sliding processes explicitly, and it was applied to the analysis of the deamination by A3G. As a result, the location-dependent deamination can be explained by a difference in the catalytic rates that depend on the direction of the approach of A3G to the target cytidine. Real-time NMR experiments also showed that A3G deaminates CCCC tandem hotspots with little redundancy, which suggests that A3G efficiently mutates many CCC hotspots that are scattered throughout the HIV-1 genome.*

The enzyme APOBEC3G (A3G) possesses two consensus zinc-finger-type cytidine deaminase motifs (CD1 and CD2),[2] but only CD2 is catalytically active.[7,8] A3G preferably deaminates the third cytidine of a CCC sequence in single-stranded DNA (ssDNA).[9,10] It was reported that A3G nonspecifically binds to ssDNA and slides along ssDNA over 30 nm (69 nucleotides) without directional preference.[11,12] Interestingly, A3G deaminates CCC hot spots in a location-dependent fashion.[10] A 5′ to 3′ gradient of mutations in HIV RNA, which is transcribed from the minus strand DNA, was observed in vivo.[9,13] This would arise from the 3′ to 5′ deamination gradient of minus strand DNA by A3G. Deamination by A3G has been analyzed by various methods, including gel shift assays,[10,14,15] single-molecule fluorescence resonance energy transfer (FRET) spectroscopy,[11] and atomic force microscopy.[12,16] We previously demonstrated that real-time NMR spectroscopy can be utilized to monitor the deamination reaction and revealed that A3G CD2 deaminates the third cytidine of CC<u>C</u> much faster than the second one (C<u>C</u>C).[17] An advantage of real-time NMR spectroscopy over other methods is that it can directly detect a site-specific deamination reaction. Moreover, this method is sensitive to weak interactions because highly concentrated ssDNA (mM order) can be used for the NMR experiment. The real-time NMR method that we used for the analysis of the deamination process has become increasingly popular and has been used by other groups.[18,19]

Our real-time NMR method monitors the intensity change of the H5–H6 total correlation spectroscopy (TOCSY) peak of the third cytidine of CC<u>C</u> in real time. Using this method, we previously analyzed the deamination of a hot spot that solely exists in ssDNA. To gain insight into the mechanism that underlies the location-dependent deamination by A3G, we further developed this NMR method. First, to determine whether real-time NMR spectroscopy provides sufficiently high spectral and time resolution to distinguish the multiple deamination reactions that occur on ssDNA, we monitored the deamination reactions of ssDNA comprising two CCC hot spots (S_{2CCC} in Table 1; see also the Supporting Information). Obviously, the two hot spots were deaminated at different rates by full-length A3G (Figure 1a). Surprisingly, CD2 alone also deaminated the two hot spots in a location-dependent manner, exhibiting higher activity than full-length A3G (Figure 1b). The higher activity of A3G CD2 was previously observed by Chen and co-workers.[14] F-tests showed that the difference between the deamination rates for

[*] Dr. A. Furukawa, Prof. T. Nagata, Prof. T. Kodaki, Prof. M. Katahira
Institute of Advanced Energy, Graduate School of Energy Science
Kyoto University
Gokasho, Uji, Kyoto 611-0011 (Japan)
E-mail: katahira@iae.kyoto-u.ac.jp
Dr. K. Sugase
Bioorganic Research Institute, Suntory Foundation for Life Sciences
1-1-1 Wakayamadai, Shimamoto, Mishima, Osaka 618-8503 (Japan)
Dr. R. Morishita
CellFree Sciences Co., Ltd., Ehime University Venture
Matsuyama, Ehime 790-8577 (Japan)
Prof. A. Takaori-Kondo
Department of Hematology and Oncology
Graduate School of Medicine, Kyoto University
54 Shogoin-Kawaracho, Sakyo-ku, Kyoto 606-8507 (Japan)
Dr. R. Morishita, Prof. A. Ryo
Department of Microbiology
Yokohama City University School of Medicine
3-9 Fukuura, Kanazawa-ku, Yokohama 236-0004 (Japan)

[**] We thank the Ministry of Education, Science, Sports and Culture of Japan for Grants-in Aid for Scientific Research (24121714, 25115507, and 25291013 to M.K.; 23570146 and 24113710 to T.N.), Japan Science and Technology (CREST; M.K.), the Sumitomo–Denko and Iwatani Foundations (M.K.), and the Japan Society for the Promotion of Science (A.F.). For funding for open access charges, we are grateful to the Ministry of Education, Science, Sports and Culture of Japan (24121714).

Supporting information for this article is available on the WWW under http://dx.doi.org/10.1002/anie.201309940.

Table 1: Oligonucleotides used in this study.

Name	Sequence
S_{2CCC}	ATTCCCAATTTTTTTTATACCCATTT
$S_{CCCssCCC}$	ATTCCCAATTTTTTTTTTTTTTTTTTTATACCCAT_{23}
$S_{CCCdsCCC}$	ATTCCCAATTCGCGAACGCGCAAGCGCATACCCAT_{23}
	GCGCTTGCGCGTTCGCG
$S_{5'CCC}$	TTACCCAT_{42}
S_{mCCC}	T_{21}ACCCAT_{22}
$S_{3'CCC}$	T_{41}ACCCATTT
S_{CCCC}	ATTCCCCATT
S_{CCCU}	ATTCCCUATT
S_{CCUC}	ATTCCUCATT
S_{CCCA}	ATTCCCAATT
S_{CCUA}	ATTCCUAATT
S_{CCUU}	ATTCCUUATT

The cytidines that are to be deaminated are underlined.

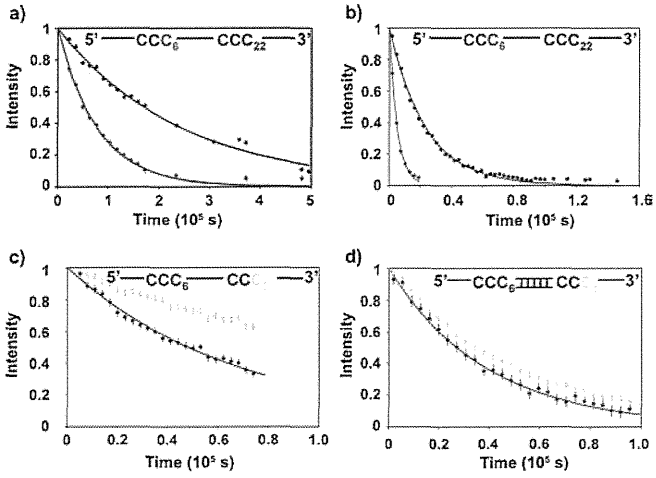

Figure 1. Real-time monitoring of deamination reactions at two CCC hot spots in ssDNA. a, b) Deamination reactions with full-length A3G (a) and CD2 (b) were monitored for C6 (●) and C22 (●) in S_{2CCC}. The deamination rates for full-length A3G are $1.3\times10^{-5}\pm4.0\times10^{-7}$ s^{-1} for C6 and $4.1\times10^{-6}\pm7.4\times10^{-8}$ s^{-1} for C22, and those for CD2 are $2.0\times10^{-4}\pm7.5\times10^{-6}$ s^{-1} for C6 and $4.2\times10^{-5}\pm5.0\times10^{-7}$ s^{-1} for C22. c, d) Deamination reactions of CD2 were monitored for C6 (●) and C33 (●) in $S_{CCCssCCC}$ (c) and $S_{CCCdsCCC}$ (d).

the two hot spots is statistically significant for both full-length A3G and CD2. The same result was obtained with ssDNA in which two units of S_{2CCC}, ATTCCCAAT and ATACCCATT, had swapped positions. These results confirmed that CD2 alone causes the location-dependent deamination. Although catalytically inactive CD1 also supposedly contributes to the location-dependent deamination process, we assumed that the intrinsic characteristics of CD2 are important for the location-dependent deamination by full-length A3G. We focused on CD2 in the following experiments. Subsequently, we investigated whether our real-time NMR method can be used to examine the sliding of A3G along ssDNA. As A3G binds to ssDNA, but not to dsDNA,[10] intervening dsDNA should block the sliding of A3G. As shown in Figure 1c and d, the deamination rates of two hot spots in a substrate with short dsDNA between them were almost the same, whereas the rates were location-dependent without dsDNA ($S_{CCCdsCCC}$ and $S_{CCCssCCC}$ in Table 1). This finding clearly indicates that real-time NMR spectroscopy can sense the sliding of A3G CD2 along ssDNA.

We have thus confirmed that real-time NMR spectroscopy is sufficiently sensitive to location-dependent deamination reactions and sliding processes of A3G CD2. Based on these results, we designed experiments and constructed a kinetic model to quantitatively analyze the deamination reaction. As A3G binds to ssDNA nonspecifically, the binding rate should depend on the length of the ssDNA and the concentrations of A3G and ssDNA. On the other hand, the duration of the sliding to reach a hot spot should depend on the length of the ssDNA and the position of a hot spot. Therefore, the kinetics of the deamination reaction can be determined by real-time NMR studies with different concentrations of ssDNA and A3G CD2, and with ssDNAs of different lengths and with different positions of hot spots. According to this idea, we developed a kinetic model for the analysis of real-time NMR data (see the Supporting Information). The deamination reaction that is monitored by NMR spectroscopy as a change of intensity, $I(t)$, is expressed as:

$$I(t) = I_0\exp(-k_{deami}t) \quad (1)$$

I_0 is the initial intensity, which is proportional to the concentration of ssDNA, and k_{deami} represents the apparent deamination rate, which is calculated as detailed below:

$$k_{deami} = \frac{[^NS][^NE]}{S_0K_d}\left\{k_{cat(3'\rightarrow5')}(1-\alpha^n) + k_{cat(5'\rightarrow3')}\left(1-\alpha^{N-n+1}\right)\right\} \quad (2)$$

$$[^NS] = \frac{1}{2}\left(-{}^N\beta + S_0 - E_0 + \sqrt{({}^N\beta - S_0 + E_0)^2 + 4E_0{}^N\beta}\right) \quad (3)$$

$$[^NE] = \frac{1}{2}\left(-{}^N\beta - S_0 + E_0 + \sqrt{({}^N\beta + S_0 - E_0)^2 + 4E_0{}^N\beta}\right) \quad (4)$$

$$\alpha = k_s/(k_s + k_{off}), \quad {}^N\beta = \frac{K_d}{2\{N+1-(1-\alpha^{N+1})/(1-\alpha)\}} \quad (5)$$

N and n represent the total number of nucleotides in ssDNA and the position of the reacting cytidine from the 3' end, respectively. According to this kinetic model, A3G CD2 binds to any nucleotide of ssDNA with an association rate constant k_{on} and dissociates from ssDNA with a dissociation rate constant k_{off}. A3G CD2 slides along ssDNA in both directions at a sliding rate k_s (Figure 2a). As the ssDNAs used are relatively short (49–57 nucleotides), we assumed that the sliding of A3G CD2 does not change direction during a single sliding event. The structure of the A3G–ssDNA complex has not been determined yet; therefore, it is still unknown how A3G recognizes a hot spot. On the other hand, the structure of free A3G CD2 has already been determined, and a protruding bump that hangs over one side of the catalytic pocket, which includes the catalytic residue Glu259 and the zinc ion, was revealed (Supporting Information, Figure S1a).[14,17,20] We assumed that this bump interferes with the accommodation of the target cytidine into the catalytic pocket; this process depends on the direction of the approach of A3G CD2 (Figure S1b,c). Then, we incorporated two cata-

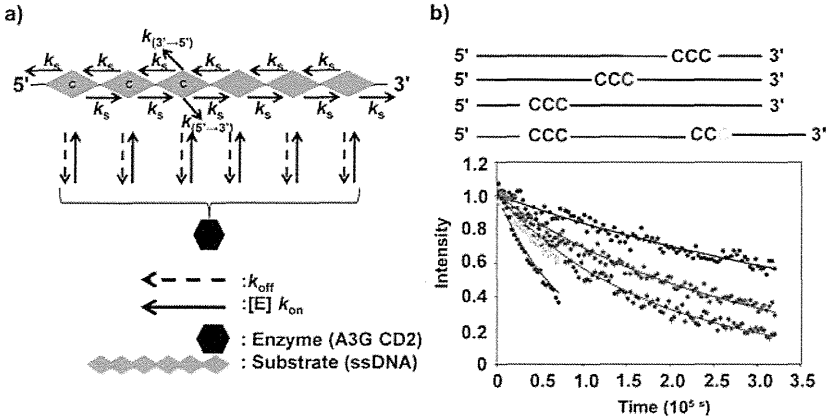

Figure 2. Quantitative analysis of the location-dependent deamination reaction using real-time NMR spectroscopy. a) Kinetic model of the deamination reaction by A3G. b) Real-time NMR data for C6 of $S_{5'CCC}$ (●), C26 of S_{mCCC} (●), C45 of $S_{3'CCC}$ (●), and both C6 (●) and C33 (●) of $S_{CCCssCCC}$ were fitted to Eq. (1).

lytic rates, $k_{cat(3'\rightarrow5')}$ and $k_{cat(5'\rightarrow3')}$, into the model, which are the catalytic rates for the cases where A3G CD2 approaches the target cytidine from downstream and upstream, respectively. As A3G slides along ssDNA without directional preference,[12] the location-dependent deamination is difficult to explain without the two different k_{cat} values. These k_{cat} values represent the rates of the entry of ssDNA into the catalytic pocket and of its deamination. A global fit of multiple real-time NMR data collected under different conditions (see above) provided the parameters α, K_d ($=k_{off}/k_{on}$), $k_{cat(3'\rightarrow5')}$, and $k_{cat(5'\rightarrow3')}$. However, it is difficult to separate α into k_s and k_{off} because neither the sliding nor the dissociation process can be perturbed experimentally without affecting the other process. The NMR data were fitted to Eq. (1) using the program GLOVE.[21]

For this analysis, we obtained real-time NMR data for $S_{5'CCC}$, S_{mCCC}, and $S_{3'CCC}$ (Table 1) aside from the data for the aforementioned two hot spots of $S_{CCCssCCC}$. These data are in good agreement with Eq. (1), yielding values for $k_{cat(3'\rightarrow5')}$ and $k_{cat(5'\rightarrow3')}$ of 68 s^{-1} and 14 s^{-1}, respectively (Figure 2b). The closer a CCC hot spot is located to the 5′ end, the more chance it has of being detected by A3G approaching from downstream rather than from upstream; therefore, a CCC hot spot that is located close to the 5′ end is deaminated more rapidly than one that is less close to the 5′ end.

For further applications of our real-time NMR method, we analyzed the deamination of CCCC, in which two CCC sequences overlap (S_{CCCC} in Table 1). The clusters of three to six consecutive cytidines are scattered throughout the HIV genome, and CCCC is the second most abundant cluster after CCC. Unfortunately, the NMR peaks that need to be monitored during the deamination reactions overlapped, for example, the TOCSY peaks of the fourth cytidines of CCCC and CCUC. Therefore, the time courses of each deamination reaction could not be monitored separately (Figure 3 a and b). However, the results of the deamination reactions were characterized using the NMR spectrum of the same ssDNA whose deamination reactions had reached completion. As a result, the third and fourth cytidines of CCCC were found to be deaminated by A3G CD2 with equal efficiency because the intensities of peaks 2 (CCUC) and 3 (CCCU + CCUU) were nearly identical. This finding is different from that of a previous study with a gel shift assay; in the earlier case, the third cytidine was deaminated more efficiently than the fourth cytidine.[15] This discrepancy could be due to the difference in the duration of the monitoring between our NMR method (6 h) and the gel shift assay (3 min). Real-time NMR spectroscopy can monitor multiple reactions directly and simultaneously using a single sample, whereas the gel shift assay cannot. Therefore, our results should provide more accurate information.

The deamination of CCCU into CCUU is redundant and may be unnecessary for abolition of the HIV infectivity. However, the above experiment could not provide information on the deamination efficiency for CCCU because the NMR peaks of CCUU and CCUC overlapped. Thus, we monitored the deamination reactions for CCCA (non-deaminated site) and CCCU (monodeaminated site) to determine whether or not A3G has a preference for either of the two sequences, S_{CCCA} and S_{CCCU} (Table 1). In this case, the deamination reactions were monitored by one-dimensional ^{1}H NMR spectroscopy to increase spectral resolution (Figure 3 c and d). The results revealed that A3G preferentially deaminates a non-deaminated site rather than a monodeami-

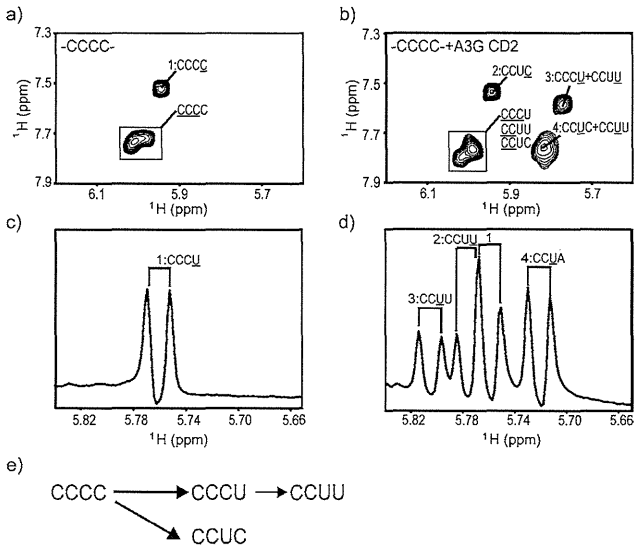

Figure 3. Deamination reactions of CCCC by A3G CD2. a, b) TOCSY spectrum of S_{CCCC} (a) and TOCSY spectrum recorded six hours after the addition of A3G CD2 (b). The peaks are labeled with the sequences of the corresponding substrates or deaminated products in which the assigned residues are underlined (see the Supporting Information). c, d) ^{1}H NMR spectrum of an equimolar mixture of S_{CCCA} and S_{CCCU} (c), and ^{1}H NMR spectrum recorded 40 minutes after the addition of A3G CD2 (d). Peaks 1 to 4 were assigned by recording the NMR spectra of S_{CCUU} and S_{CCUA}. e) Two possible deamination reaction pathways for CCCC.

nated site because the intensity of the peak for the deaminated product CCUA (peak 4) was greater than that of the peak corresponding to CCUU (peak 3). A3G would exploit this sequential preference to efficiently deaminate multiple hot spots that are scattered throughout the HIV genome with a small amount of redundant deamination of CCCC.

In conclusion, we analyzed real-time NMR data for the location-dependent deamination by A3G CD2 using a newly derived kinetic model. As a result, the location-dependent deamination can be explained by the difference in the rate constants k_{cat} of CD2, which depend on the direction of the approach to the target cytidine. We also characterized deamination reactions of CCCC by real-time NMR spectroscopy, even though multiple reactions occurred simultaneously. Previously, it was proposed that the location-dependent deamination is caused by two binding orientations on ssDNA and the existence of a region where either less or no deamination occurs (ca. 30 nucleotides) at the 3′ end of the ssDNA.[10,16] However, this model cannot explain the location-dependent deamination that is observed for long ssDNA (70 nucleotides)[15] because the contribution of the dead region to the location dependency becomes smaller. On the other hand, our model can explain the location-dependent deamination reaction even for such a long ssDNA fragment.

Recently, it was proposed that the proteins of the APOBEC family are involved in epigenesis.[22] They may contribute to the removal of an epigenetic marker, a methyl group of a 5-methyl cytosine, through deamination of 5-hydroxymethyl cytosine. Our real-time NMR method could also be applied to examine such DNA modifications and to provide insight into epigenesis. Furthermore, this method can also be used for the analysis of post-translation modifications of proteins.

Received: November 15, 2013
Published online: January 29, 2014

Keywords: deamination · DNA · enzyme kinetics · quantitative analysis · NMR spectroscopy

[1] A. M. Sheehy, N. C. Gaddis, J. D. Choi, M. H. Malim, *Nature* **2002**, *418*, 646–650.
[2] R. S. Harris, M. T. Liddament, *Nat. Rev. Immunol.* **2004**, *4*, 868–877.
[3] D. Lecossier, F. Bouchonnet, F. Clavel, A. J. Hance, *Science* **2003**, *300*, 1112.
[4] B. Mangeat, P. Turelli, G. Caron, M. Friedli, L. Perrin, D. Trono, *Nature* **2003**, *424*, 99–103.
[5] H. Zhang, B. Yang, R. J. Pomerantz, C. Zhang, S. C. Arunachalam, L. Gao, *Nature* **2003**, *424*, 94–98.
[6] R. S. Harris, K. N. Bishop, A. M. Sheehy, H. M. Craig, S. K. Petersen-Mahrt, I. N. Watt, M. S. Neuberger, M. H. Malim, *Cell* **2003**, *113*, 803–809.
[7] G. Hache, M. T. Liddament, R. S. Harris, *J. Biol. Chem.* **2005**, *280*, 10920–10924.
[8] F. Navarro, B. Bollman, H. Chen, R. Konig, Q. Yu, K. Chiles, N. R. Landau, *Virology* **2005**, *333*, 374–386.
[9] Q. Yu, R. Konig, S. Pillai, K. Chiles, M. Kearney, S. Palmer, D. Richman, J. M. Coffin, N. R. Landau, *Nat. Struct. Mol. Biol.* **2004**, *11*, 435–442.
[10] L. Chelico, P. Pham, P. Calabrese, M. F. Goodman, *Nat. Struct. Mol. Biol.* **2006**, *13*, 392–399.
[11] L. S. Shlyakhtenko, A. Y. Lushnikov, A. Miyagi, M. Li, R. S. Harris, Y. L. Lyubchenko, *Biochemistry* **2012**, *51*, 6432–6440.
[12] G. Senavirathne, M. Jaszczur, P. A. Auerbach, T. G. Upton, L. Chelico, M. F. Goodman, D. Rueda, *J. Biol. Chem.* **2012**, *287*, 15826–15835.
[13] R. Suspène, C. Rusniok, J. P. Vartanian, S. Wain-Hobson, *Nucleic Acids Res.* **2006**, *34*, 4677–4684.
[14] L. G. Holden, C. Prochnow, Y. P. Chang, R. Bransteitter, L. Chelico, U. Sen, R. C. Stevens, M. F. Goodman, X. S. Chen, *Nature* **2008**, *456*, 121–124.
[15] R. Nowarski, E. Britan-Rosich, T. Shiloach, M. Kotler, *Nat. Struct. Mol. Biol.* **2008**, *15*, 1059–1066.
[16] L. Chelico, C. Prochnow, D. A. Erie, X. S. Chen, M. F. Goodman, *J. Biol. Chem.* **2010**, *285*, 16195–16205.
[17] A. Furukawa, T. Nagata, A. Matsugami, Y. Habu, R. Sugiyama, F. Hayashi, N. Kobayashi, S. Yokoyama, H. Takaku, M. Katahira, *EMBO J.* **2009**, *28*, 440–451.
[18] S. Harjes, W. C. Solomon, M. Li, K. M. Chen, E. Harjes, R. S. Harris, H. Matsuo, *J. Virol.* **2013**, *87*, 7008–7014.
[19] I. J. Byeon, J. Ahn, M. Mitra, C. H. Byeon, K. Hercik, J. Hritz, L. M. Charlton, J. G. Levin, A. M. Gronenborn, *Nat. Commun.* **2013**, *4*, 1890.
[20] K. M. Chen, E. Harjes, P. J. Gross, A. Fahmy, Y. Lu, K. Shindo, R. S. Harris, H. Matsuo, *Nature* **2008**, *452*, 116–119.
[21] K. Sugase, T. Konuma, J. C. Lansing, P. E. Wright, *J. Biomol. NMR* **2013**, *56*, 275–283.
[22] N. Bhutani, D. M. Burns, H. M. Blau, *Cell* **2011**, *146*, 866–872.

EUROPEAN JOURNAL OF Haematology

European Journal of Haematology 92 (219–228)

ORIGINAL ARTICLE

Antitumor effects of bevacizumab in a microenvironment-dependent human adult T-cell leukemia/lymphoma mouse model

Fumiko Mori[1], Takashi Ishida[1], Asahi Ito[1], Fumihiko Sato[2], Ayako Masaki[1], Tomoko Narita[1], Susumu Suzuki[2], Tomiko Yamada[1], Hisashi Takino[2], Masaki Ri[1], Shigeru Kusumoto[1], Hirokazu Komatsu[1], Masakatsu Hishizawa[3], Kazunori Imada[4], Akifumi Takaori-Kondo[3], Akio Niimi[1], Ryuzo Ueda[5], Hiroshi Inagaki[2], Shinsuke Iida[1]

[1]Department of Medical Oncology and Immunology, Nagoya City University Graduate School of Medical Sciences, Nagoya;[2]Department of Anatomic Pathology and Molecular Diagnostics, Nagoya City University Graduate School of Medical Sciences, Nagoya; [3]Department of Hematology and Oncology, Graduate School of Medicine, Kyoto University, Kyoto; [4]Department of Hematology, Kokura Memorial Hospital, Kitakyushu; [5]Department of Tumor Immunology, Aichi Medical University School of Medicine, Nagakute, Japan

Abstract

Objective: The objective of this study was to evaluate the therapeutic potential of bevacizumab with or without systemic chemotherapy for adult T-cell leukemia/lymphoma (ATL) and clarify the significance of angiogenesis for ATL pathogenesis. *Methods:* NOD/Shi-*scid*, IL-2Rγ^{null} (NOG) mice were used as recipients of tumor cells from a patient with ATL, which engraft and proliferate in a microenvironment-dependent manner. The ATL cells could be serially transplanted in NOG mice, but could not be maintained in *in vitro* cultures. *Results:* Injection of bevacizumab alone significantly increased necrosis and decreased vascularization in the tumor tissue. Levels of human soluble interleukin two receptor in the serum (reflecting the ATL tumor burden) of bevacizumab-treated mice were significantly lower than in untreated mice. Although bevacizumab monotherapy showed these clear anti-angiogenesis effects, it did not prolong survival. In contrast, injection of bevacizumab together with cyclophosphamide, doxorubicin, vincristine, prednisolone (CHOP) led to a significant prolongation of survival of the ATL mice relative to CHOP alone. *Conclusions:* This is the first report to evaluate the efficacy of bevacizumab for ATL in a tumor microenvironment-dependent model. Bevacizumab therapy combined with chemotherapy could be a valuable treatment strategy for that subgroup of ATL probably depending to a large extent on angiogenesis via vascular endothelial growth factor.

Key words Adult T-cell leukemia-lymphoma; Bevacizumab; tumor microenvironment

Correspondence Takashi Ishida, MD, PhD, Department of Medical Oncology and Immunology, Nagoya City University Graduate School of Medical Sciences, 1 Kawasumi, Mizuho-chou, Mizuho-ku, Nagoya, Aichi 467-8601, Japan. Tel: +81 52 853 8216; Fax: +81 52 852 0849; e-mail: itakashi@med.nagoya-cu.ac.jp

Accepted for publication 29 October 2013

doi:10.1111/ejh.12231

Adult T-cell leukemia-lymphoma (ATL) is an aggressive peripheral T-cell neoplasm caused by human T-cell lymphotropic virus type 1 (HTLV-1). The disease is resistant to conventional chemotherapeutic agents, and currently there are only limited treatment options; thus, it has a very poor prognosis (1–4). Over the past decade, allogeneic hematopoietic stem-cell transplantation has evolved into a potential approach to treating patients with ATL. However, only a small fraction of patients have the opportunity to benefit from transplantation, such as those who are younger, have achieved sufficient disease control, and have an appropriate stem-cell source (5, 6). Therefore, the development of alternative treatment strategies for patients with ATL is an urgent issue.

Bevacizumab is a humanized monoclonal antibody against the vascular endothelial growth factor A (VEGF-A), a key

factor inducing the formation of blood vessels (angiogenesis) in tumors (7). Bevacizumab is currently approved worldwide for the treatment of several types of cancer such as metastatic colorectal cancer, metastatic non-small-cell lung cancer, renal cell carcinoma, and advanced ovarian cancer, in combination with chemotherapy or interferon (8–14). Bevacizumab is also approved as a single agent for recurrent glioblastoma in the USA (15). In this context, many aspects of pathological angiogenesis have been extensively studied in many types of cancer. On the other hand, the precise role of these processes in pathogenesis of hematological malignancies including ATL is still under active investigation (16–19). Thus far, bevacizumab has not been approved for the treatment of any hematological malignancy in the USA, Europe, or Japan. The aim of the present study was to evaluate the therapeutic potential of bevacizumab with or without systemic chemotherapy for ATL and clarify the significance of angiogenesis for ATL pathogenesis, using a microenvironment-dependent murine ATL model.

Methods

Animals

NOD/Shi-*scid*, IL-2Rγ^{null} (NOG) mice (20) were purchased from the Central Institute for Experimental Animals (Kanagawa, Japan) and used at 6–8 wk of age. All of the *in vivo* experiments were performed in accordance with the United Kingdom Coordinating Committee on Cancer Research Guidelines for the Welfare of Animals in Experimental Neoplasia, Second Edition, and were approved by the Ethics Committee of the Center for Experimental Animal Science, Nagoya City University Graduate School of Medical Sciences.

Immunopathological analysis

We assessed the affected lymph nodes of 23 patients with ATL by immunopathology. The patients provided written informed consent in accordance with the Declaration of Helsinki, and this present study was approved by the institutional Ethics Committee of Nagoya City University Graduate School of Medical Sciences. Hematoxylin and eosin (HE) staining and immunostaining using anti-human CD4 (4B12; Novocastra, Wetzlar, Germany), CD25 (4C9; Novocastra), CD20 (L26; DAKO, Glostrup, Denmark), VEGF-A (sc-152, rabbit polyclonal; Santa Cruz, Heidelberg, Germany), Alpha-Smooth Muscle Actin (α-SMA) (1A4; DAKO), CD31 (JC70A; DAKO), and von Willebrand Factor (Rabbit polyclonal; DAKO) were performed on formalin-fixed, paraffin-embedded sections. VEGF-A expression levels were categorized according to the following formula: 3+ positive if ≥50%, 2+ positive if <50 ≥30%, 1+ positive if <30 ≥10%, and negative if <10% of the ATL tumor cells were stained with the corresponding antibody. Nine 100× high-power fields (HPF) of HE tumor specimens were randomly selected, and the area of tumor necrosis (%) was calculated by Image J software (21), and then averaged. Nine 100× HPF of von Willebrand Factor-stained tumor specimens were randomly selected, and numbers of vessels (per mm^2) were calculated by Image J software and then averaged.

ATL mouse model

A leukemic cell clone from a patient with ATL, which could be serially transplanted into SCID mice, designated S-YU as reported previously (22), was injected intraperitoneally (i.p.) into NOG mice. Three to 4 wk after i.p. injection, NOG mice were presented with intraperitoneal masses along the mesentery. Cells from these intraperitoneal masses were suspended in RPMI-1640 and inoculated i.p. into healthy NOG mice, which then presented with features identical to those of the original mice.

Cell lines

ATN-1, MT-1, and TL-Om1 are ATL cell lines, whereas MT-2, MT-4, and TL-Su are HTLV-1-immortalized lines, as previously described (23).

Quantitative reverse transcription-polymerase chain reaction

Total RNA was isolated with RNeasy Mini Kits (QIAGEN, Tokyo, Japan). Reverse transcription from the RNA to first strand cDNA was carried out using High Capacity RNA-to-cDNA Kits (Applied Biosystems Inc, Foster City, CA, USA). *Human VEGF-A* (Hs00900055_m1), *VEGF-R1* (Hs00176573_m1), *VEGF-R2* (Hs00911700_m1), and *β-actin* (Hs99999903_m1) *mRNA* were amplified using TaqMan® Gene Expression Assays with the aid of an Applied Biosystems StepOnePlus™. The quantitative assessment of the mRNA of interest was done by dividing its level by that of *β-actin* and expressing the result relative to Human Testis Total RNA (Clontech, Mountain View, CA, USA) as 1.0. All expressed values were averages of triplicate experiments.

Monoclonal antibodies and flow cytometry

The following Monoclonal antibodies (mAbs) were used for flow cytometry: APC-conjugated anti-human CD45 mAb (2D1; BD Biosciences, San Jose, CA, USA), PerCP-conjugated anti-CD4 mAb (SK3; BD Biosciences), PE-conjugated anti-CD25 mAb (M-A251; BD Biosciences), PE-conjugated VEGF-R1 mAb (49560; BD Biosciences), PE-conjugated VEGF-R2 mAb (89106, R&D Systems, Inc. Minneapolis, MN,

USA), and the appropriate isotype control mAbs. Whole blood was treated with BD FACS lysing solution (BD Biosciences) to remove RBC. Stained cells were analyzed on a FACSCalibur (BD Biosciences) with the aid of FlowJo software (Tree Star, Inc. Ashland, OR, USA).

Cell proliferation assay

Proliferation of S-YU and HTLV-I-immortalized lines expressing both VEGF-A and VEGF-R1 in the presence of different concentrations of bevacizumab for 48 h was assessed using CellTiter 96 Aqueous One Solution cell proliferation assay kits (Promega Corporation, Madison, WI, USA). Bevacizumab was purchased from Chugai Pharmaceutical Co., Ltd., Tokyo, Japan.

ATL cell-bearing mice treated with bevacizumab

ATL tumor cells (S-YU) from the intraperitoneal masses were suspended in RPMI-1640, and 1.0×10^7 was inoculated i.p. into each of 14 NOG mice. The animals were divided into two groups of seven each for treatment with bevacizumab or to serve as controls. Bevacizumab (10 mg/kg) or vehicle (saline) was i.p. injected into the mice 3, 10, and 17 d after tumor cell inoculations. Therapeutic efficacies were evaluated for area of tumor necrosis, number of vessels, and serum human sIL2R levels 22 d after tumor inoculation. The concentration of human sIL2R in the serum was measured by ELISA using human sIL2R immunoassay kits (R&D Systems, Inc.).

ATL cells from the intraperitoneal masses suspended in RPMI-1640 were also inoculated i.p. into another 10 NOG mice at 1.0×10^7 per mouse. These animals were randomly divided into two groups of five each for treatment with bevacizumab or as controls. Bevacizumab (10 mg/kg) or saline was injected i.p. into the mice 2, 9, 16, and 23 d after tumor cell inoculation. Therapeutic efficacy of bevacizumab was evaluated by survival times.

A further 16 NOG mice that had also received 1.0×10^7 ATL cells from intraperitoneal masses were randomly divided into two groups of eight each for treatment with bevacizumab + cyclophosphamide, doxorubicin, vincristine, prednisolone (CHOP) or CHOP alone. Bevacizumab (10 mg/kg) or saline was i.p. injected into the mice 2, 9, 16, 23, 30, and 37 d after tumor cell inoculations. CHOP was given i.p. 17 d after tumor inoculation at the following doses: cyclophosphamide, 40 mg/kg; doxorubicin, 3.3 mg/kg; vincristine, 0.5 mg/kg; and prednisolone, 0.2 mg/kg (24, 25). Therapeutic efficacy of bevacizumab was evaluated by survival time. Cyclophosphamide and vincristine were purchased from Shionogi Pharmaceutical Co., Ltd, Osaka, Japan; doxorubicin was from Kyowa Hakko Kirin Co., Ltd, Tokyo, Japan, and prednisolone was from Nippon Kayaku Co., Ltd, Tokyo, Japan.

Statistical analysis

The differences between groups regarding the tumor necrosis area, vascular number, and human sIL2R concentrations in serum were analyzed by the Mann–Whitney U test. In this study, $P < 0.05$ was considered significant.

Results

VEGF-A expression in ATL

VEGF-A expression by ATL cells in the lymph node lesions is shown in Fig. 1A. Immunopathological features of four cases from each group stratified by VEGF-A expression are shown in Fig. 1B. Most of the ATL cases (96%) were positive for VEGF-A.

ATL cell-bearing NOG mice

In earlier studies, S-YU ATL tumor cells, which were serially transplanted into SCID mice (22), manifested multiple enlarged mesenteric lymph nodes. In the present study, in which NOG mice rather than SCID mice were the S-YU recipients, larger tumor masses formed along the intestinal tract. Figure 2A shows the intraperitoneal masses and intestinal tract adhering tightly to one another in a NOG mouse (demarcated by thin white dotted lines in the figure). Flow cytometric analysis demonstrated that the mass mainly consisted of human cells expressing CD4 and CD25 (Fig. 2B). Immunopathological analysis revealed large atypical cells with irregular and pleomorphic nuclei, and blood vessels. The cells were CD4-positive, CD25-positive, but CD20-negative (Fig. 2C). These findings are consistent with an ATL cell phenotype in humans, and with earlier studies in the SCID/S-YU model. The S-YU tumor cells in the NOG mice were classed as VEGF-A 1+ positive (Fig. 2C). Blood vessels in the tumor tissue were stained by anti-α-SMA Ab (Fig. 2C). Vascular endothelial cells in the tumor tissue were stained by anti-von Willebrand Factor Ab, but not by anti-CD31 mAb (data not shown). Together, these results show that the blood vessels in the tumor tissue originated from the mouse, because anti-α-SMA and von Willebrand Factor Ab used in this study recognized the corresponding protein derived from both human and mouse, whereas the anti-CD31 mAb recognized the corresponding human but not murine protein (data not shown). CD4-positive CD25-positive ATL cell mild infiltration into spleen, liver, and bone marrow was seen by flow cytometry (Fig. 2D).

VEGF-A, VEGF-R1, and -R2 expression in ATL and HTLV-1-immortalized lines

VEGF-A mRNA expression was detected in all 7 ATL and HTLV-1-immortalized lines tested, and in S-YU cells

A

VEGF-A expression

Negative	Positive			
(–)	(1+)	(2+)	(3+)	
1 (4)	9 (39)	9 (39)	4 (17)	n (%)

B

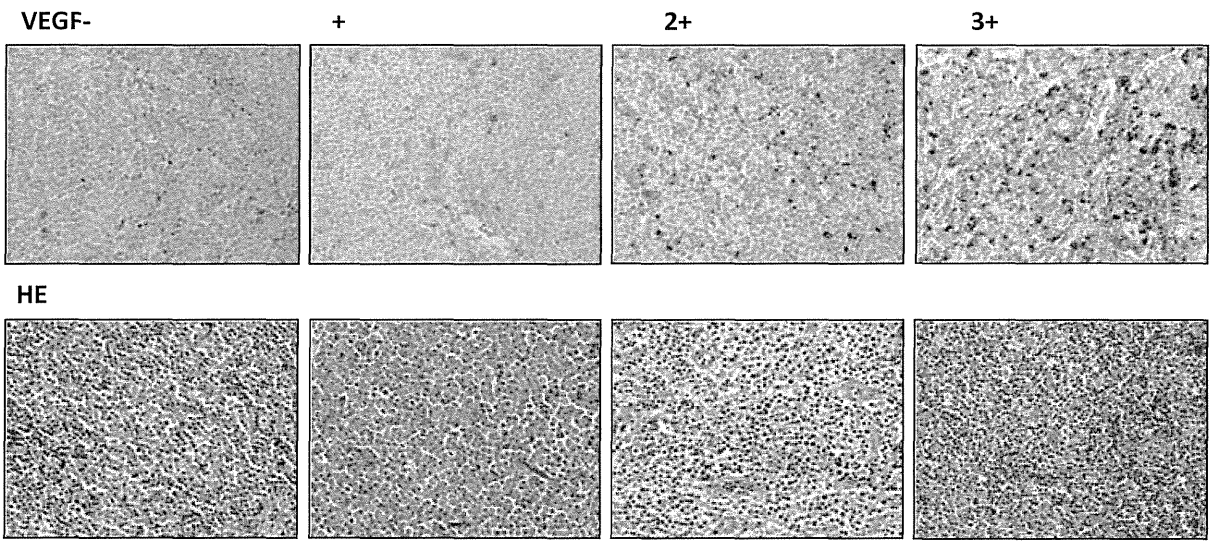

Figure 1 Vascular endothelial growth factor A (VEGF-A) expression in ATL. (A) VEGF-A expression of ATL cells in the lymph node lesion. VEGF-A expression was categorized based on the percentage of ATL cells stained as follows: ≥50%, 3+ positive; 30–49%, 2+ positive; 10–29%, 1+ positive; <10%, negative. (B) Cases 1, 2, 3, and 4 are representative of VEGF-A-negative, 1+, 2+, and 3+ positive categories, respectively. Photomicrographs with VEGF-A (upper panels) and hematoxylin and eosin staining (lower panels) are shown.

from intraperitoneal masses (Fig. 3A, upper left panel). *VEGF-R1 mRNA* expression was not present in ATL and in only two HTLV-1-immortalized lines (MT-2 and TL-Su) but was present in S-YU cells (Fig. 3A, upper right panel). No *VEGF-R2 mRNA* expression was detected in any of the 7 ATL and HTLV-1-immortalized lines tested, or in S-YU cells (data not shown). Flow cytometry demonstrated that VEGF-R1 protein was also expressed in MT-2 and TL-Su, and very weakly in NOG S-YU cells (Fig. 3A, lower panels), consistent with the RT-PCR results. Flow cytometry demonstrated that VEGF-R2 was not expressed at all in any of the ATL and HTLV-1-immortalized lines tested, or in S-YU cells (data not shown), which was also consistent with the RT-PCR results.

VEGF-R1 and VEGF-R2 expression in primary ATL cells

CD4-positive CD25-positive primary ATL cells in PBMC obtained from nine individual patients with ATL (i–ix) were evaluated for VEGF-R1 and -R2 expression. VEGF-R1 protein was expressed in only one patient (patient v) and VEGF-R2 was not expressed in any of the patients (Fig. 4B).

No Bevacizumab-mediated anti-proliferative activity against HTLV-1-immortalized lines and S-YU *in vitro*

Bevacizumab did not directly block the proliferation of MT-2 and TL-Su cells *in vitro*, despite their expression of both VEGF-A and VEGF-R1. Neither did it inhibit S-YU cells (Fig. 3C).

Therapeutic efficacy of bevacizumab monotherapy in S-YU cell-bearing NOG mice

Photomicrographs of tumor tissue from each mouse are shown (Fig. 4A). Treatment with bevacizumab resulted in an increased percentage of tumor necrosis in the NOG/S-YU mice (mean 25.3%, median 24.1%, range 19.2–33.6%), compared to control mice (mean 15.9%, median 15.4%, range 11.7–21.0%, $P = 0.0060$) (Fig. 4B, left panel). An example of calculating the percentage necrotic area is presented in Fig. 4B, right-hand panels. Bevacizumab treatment resulted in decreased vascular number in the tumor tissues [3.1, 2.6,

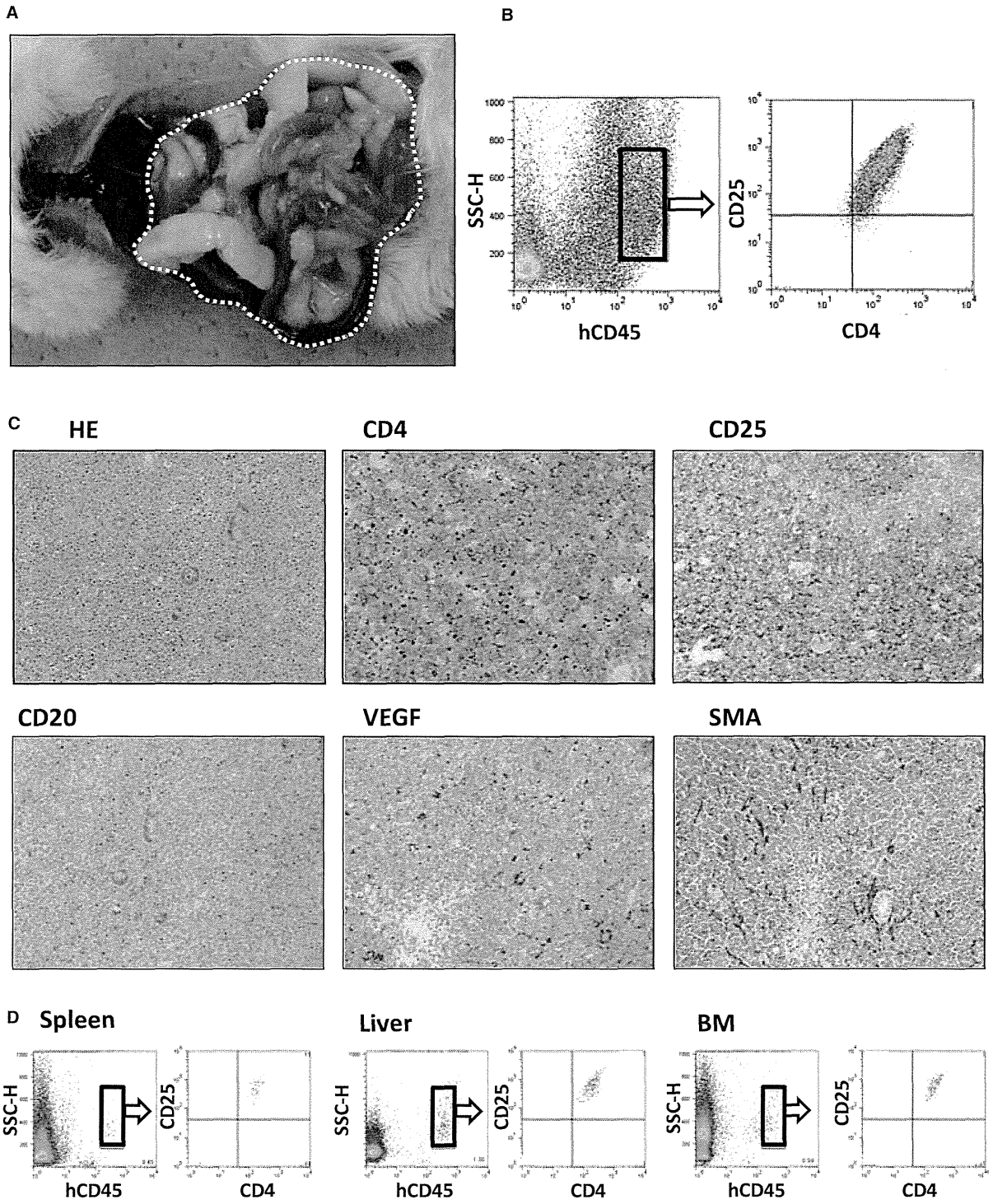

Figure 2 ATL cell-bearing NOG mouse model. (A) Macroscopic appearance of a primary DLBCL cell-bearing ATL mouse. The intraperitoneal mass is demarcated by a thin white dotted line. (B) Human CD45-positive cells in the mass determined by human CD4 and CD25 expression. (C) Immunohistochemical images of the intraperitoneal mass. (D) Human CD45-positive cells of each organ determined by human CD4 and CD25 expression.

0.0–8.3/mm^2; (mean, median, range)], compared to controls (12.8, 15.6, 1.6–19.3/mm^2, $P = 0.0127$) (Fig. 4C, left panel). An example of this calculation is presented in Fig. 4C, right-hand panels. Because sIL2R appears in the serum, concomitant with its increased expression on cells, we measured human sIL2R concentrations as a surrogate marker reflecting

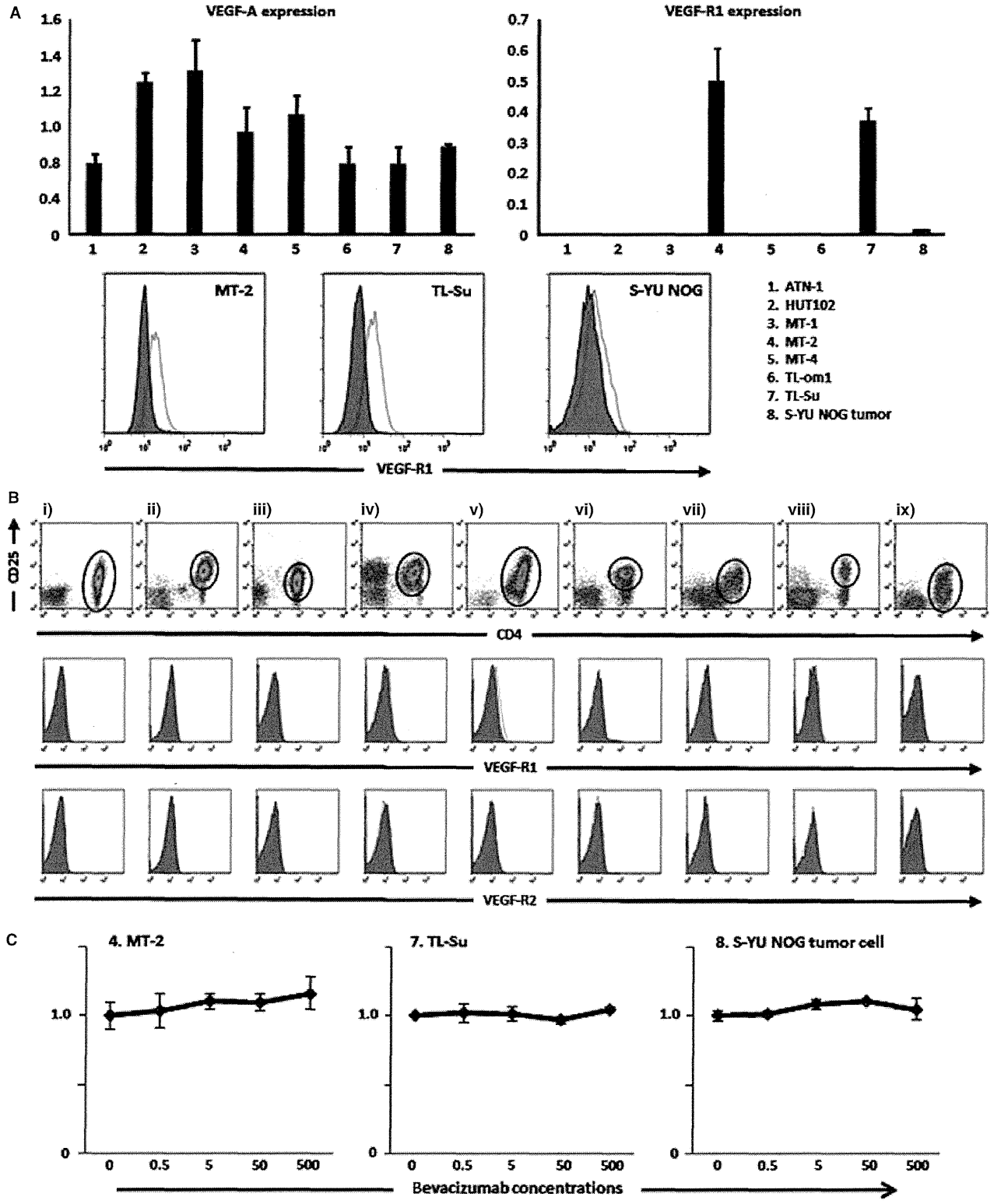

Figure 3 Vascular endothelial growth factor A (VEGF-A), VEGF-R1, and -R2 expression in primary ATL cells, or ATL and HTLV-1-immortalized lines (A) Quantitative RT-PCR analysis for VEGF-A and VEGF-R1 in 7 ATL and HTLV-1-immortalized lines, and NOG ATL cells from the intraperitoneal mass (upper panels). Flow cytometry for VEGF-R1 in HTLV-1-immortalized lines MT-2 and TL-Su, and NOG ATL cells, from the intraperitoneal mass (lower panels). (B) Flow cytometry for VEGF-R1, and -R2 in 9 primary ATL cells. (C) Bevacizumab has no direct anti-proliferative activity against HTLV-1-immortalized lines (MT-2 and TL-Su) expressing both VEGF-A and VEGF-R1, or NOG ATL cells, *in vitro*. Each result represents three independent experiments.

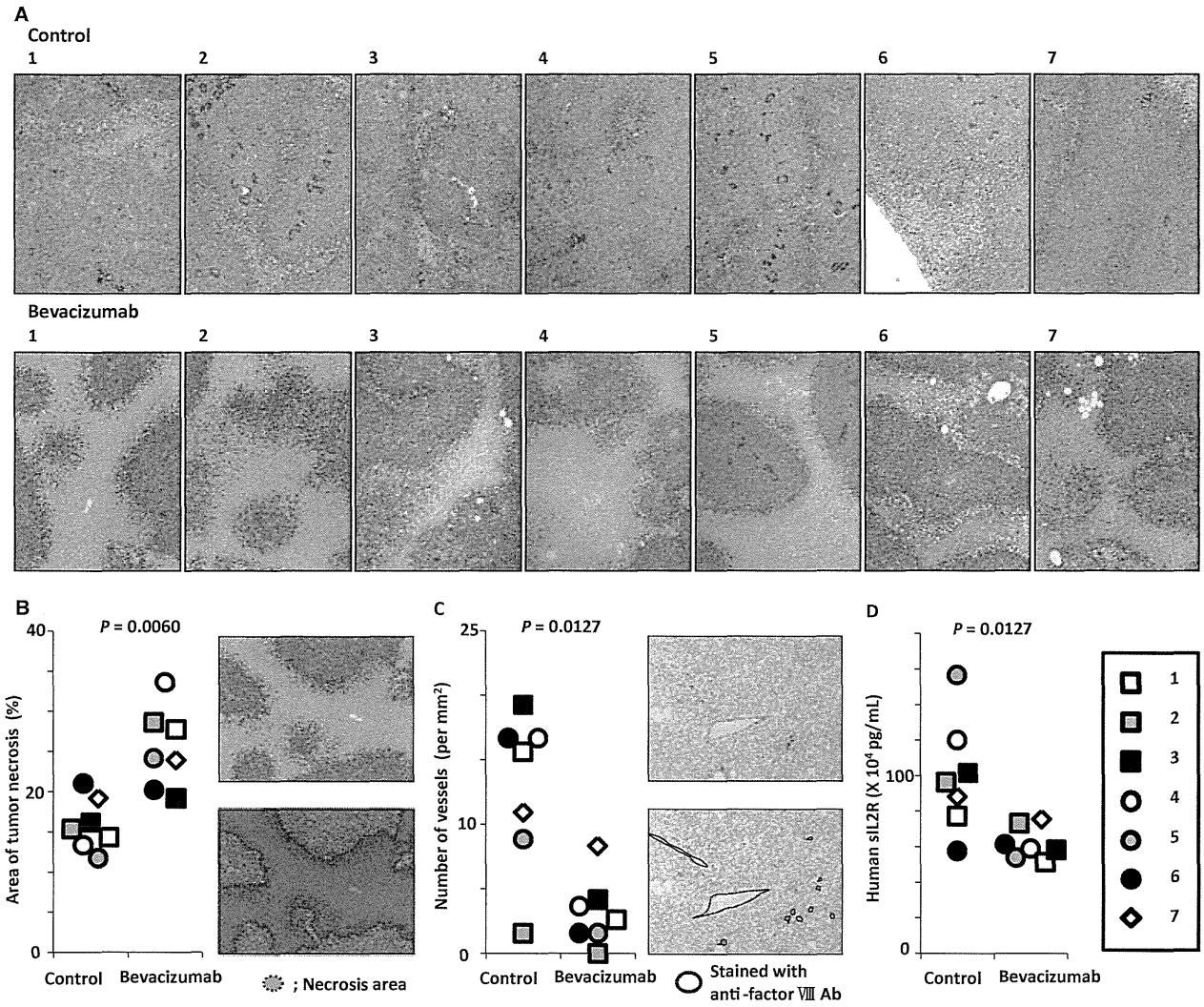

Figure 4 Bevacizumab therapy has significant therapeutic efficacy in the ATL cell-bearing NOG mouse model. (A) Macroscopic photomicrographs with hematoxylin and eosin staining of mice given saline (control) (upper panels) or bevacizumab (lower panels). (B) Area of tumor necrosis (%) of each ATL cell-bearing NOG mouse. The bevacizumab-treated mice had significantly greater tumor necrosis than control mice (left panel). An example of a calculation for tumor necrosis area (%) by means of Image J software is shown (right panels). (C) Numbers of vessels (/mm^2) of each ATL cell-bearing NOG mouse. The bevacizumab recipients had significantly fewer vessels than controls (left panel). An example of such a calculation by means of Image J software is shown (right panels). (D) Serum sIL2R concentrations of each ATL cell-bearing NOG mouse. The bevacizumab recipients had significantly lower levels of sIL2R than controls.

the tumor burden of the human CD25-expressing ATL (26). Treatment with bevacizumab showed significantly greater therapeutic efficacy as demonstrated by sIL2R concentrations in S-YU cell-bearing NOG mice (617.9, 588.5, 513.2–755.7 $\times$ 10^3 pg/mL), compared to controls (996.6, 963.4, 575.7–1565.0 $\times$ 10^3 pg/mL, P = 0.0127) (Fig. 4D). Although bevacizumab monotherapy showed significant therapeutic efficacy as demonstrated by the percentage of tumor necrosis, vascular number in the tumor tissues, and sIL2R concentrations in sera (Fig. 4), it did not confer any survival advantage to the NOG/S-YU mice (Fig. 5A). No toxicity attributable to bevacizumab injections was observed in any of the mice in this setting.

Therapeutic efficacy of bevacizumab plus CHOP compared to CHOP alone in S-YU cell-bearing NOG mice

The bevacizumab plus CHOP group did have a significant prolongation of survival compared with CHOP alone (P = 0.046). The median survival time of bevacizumab plus CHOP and CHOP alone was 38 and 34 d, respectively.

Discussion

In this study, we have demonstrated that bevacizumab possesses significant therapeutic efficacy in an ATL mouse model in which the tumor cells from a patient survive and

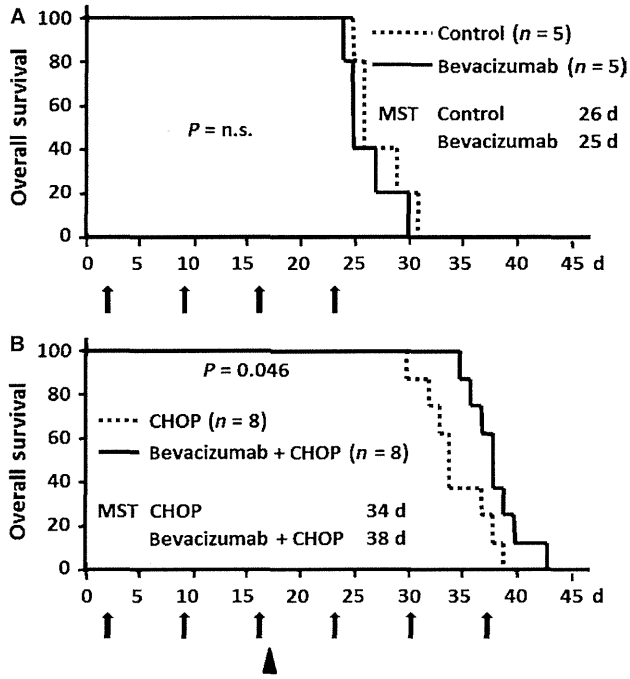

Figure 5 Survival analysis of ATL cell-bearing NOG mice treated with bevacizumab (A) Kaplan–Meier survival curves of ATL cell-bearing NOG mice treated with bevacizumab or saline. Arrows, bevacizumab or control (saline) injections. Each group consists of five mice. The difference between the bevacizumab and control groups is not significant. (B) Kaplan–Meier survival curves of ATL cell-bearing NOG mice treated with bevacizumab + CHOP, or CHOP alone. Arrows, bevacizumab or control (saline) injections. Arrow head, CHOP injection. Each group consists of eight mice. The difference between the bevacizumab + CHOP and CHOP alone is statistically significant.

proliferate in a murine microenvironment-dependent manner. The present finding revealed the importance of angiogenesis for the pathogenesis of VEGF-expressing ATL.

NOG mice have severe, multiple immune defects, such that human immune cells engrafted into them retain essentially the same functions as in humans (27, 28). While it has been reported that S-YU cells can be serially transplanted into SCID mice as recipients, the present study demonstrated that S-YU cells could also be serially transplanted into NOG mice. This was not unexpected given the even more severe immune dysfunction of NOG mice compared to SCID mice. This may also explain why the ATL tumor masses were much larger in NOG than in SCID mice.

In this study, most primary ATL cases (22/23), and all of the established cell lines tested (7/7), were positive for VEGF-A. These results are consistent with data from other investigators (16, 18, 19). Thus, the VEGF-A produced by ATL cells is likely to play an important role in the pathogenesis of ATL. On the other hand, *VEGF-R1 mRNA* expression was only seen in two of the seven ATL and HTLV-1-immortalized lines, and *VEGF–R2* in none of them. VEGF-R1 protein expression by primary ATL tumor cells was only seen in one of nine patients, and VEGF-R2 in none. In B-cell lymphomas, an earlier study reported that tumor cell growth was promoted in an autocrine fashion via VEGF-A/VEGF-R1 or VEGF-A/VEGF-R2 interactions (29). However, the present analysis of VEGF-R1/R2 expression in ATL, and the results of *in vitro* proliferation assays, did not support the existence of such an autocrine loop in ATL.

Because S-YU cells can only be maintained by serial transplantation in immunodeficient mice, but not by *in vitro* culture (30), the microenvironment is likely to be indispensable for their survival. S-YU are positive for VEGF-A, and therefore it would be expected that the interaction of VEGF-A produced by ATL cells with receptors on host (murine) endothelial cells should play an important role in tumor angiogenesis. This would lead to tumor cell survival and proliferation supported by transport of sufficient nutrients and oxygen in the mouse. Therefore, the present ATL model using S-YU should better reflect the human ATL *in vivo* environment, compared to other mouse models using established ATL cell lines, or HTLV-1-immortalized lines. Thus, this model should provide a powerful tool for understanding the pathogenesis of ATL. Furthermore, it should be useful not only for evaluating novel cytotoxic anti-ATL agents, but also provide a more appropriate *in vivo* model to test antitumor agents targeting the microenvironment, including bevacizumab.

The effect observed in mice receiving bevacizumab monotherapy, as demonstrated by the increased tumor necrosis area and reduced vasculature in the tumor tissue, was expected, given the conventional antitumor mechanism of bevacizumab, which neutralizes the human VEGF-A produced by the tumor cells, but not murine VEGF-A (31). It then inhibits the growth of new blood vessels and thus starves tumor cells of necessary nutrients and oxygen (32). This should lead to a reduced tumor burden, as indicated by the sIL2R concentrations measured. Although bevacizumab monotherapy did show this anti-angiogenesis effect, it did not lead to survival prolongation in this study. This finding is consistent with the clinical observations in many types of cancer such as colorectal cancer, non-small-cell lung cancer, renal cell carcinoma, and ovarian cancer. On the other hand, combination treatment with bevacizumab and CHOP did prolong survival compared to CHOP alone. Nonetheless, the extent of this prolongation was not marked, which is also consistent with clinical observations in many types of cancer where bevacizumab is of limited benefit and then only when combined with chemotherapy. This study suggested that the tumor cell 'starvation effect' alone mediated by bevacizumab does not result in prolonged survival. It has been reported that VEGF-targeted therapy can 'normalize' the tumor vascular network and that this can lead to a more uniform blood flow, with subsequent increased delivery of chemotherapeutic agents (33, 34). This normalization by bevacizumab is a possible explanation for the prolonged survival in the present combination setting.

The present study demonstrated the importance of angiogenesis for the pathogenesis of ATL and the potential efficacy of blocking this in at least a subgroup of patients with ATL. In recent clinical cancer therapy experience, the epidermal growth factor receptor (EGFR) tyrosine kinase inhibitor, gefitinib, failed to yield significantly improved overall survival in patients with refractory NSCLC, but did show therapeutic benefit in a subgroup of patients with mutated EGFR (35). In the case of mAb targeting the EGFR, both panitumumab and cetuximab also yield clinical benefits only in a subgroup of colorectal cancer patients with wild-type *KRAS* and BRAF (36). These findings indicate that we should develop novel treatment strategies based on tumor biology, and not on tumor category. Therefore, as a next step, further investigations are warranted to determine which subgroups of patients with ATL will benefit from bevacizumab therapy (37). In other words, we should face the challenge of developing robust biomarkers that can guide selection of those patients with ATL for whom bevacizumab therapy will be most beneficial. In addition, several promising new agents for treating ATL are currently being developed (1, 38–40). Investigations of combinations of bevacizumab with these novel agents are also warranted.

In conclusion, to the best of our knowledge this is the first report to evaluate the efficacy of bevacizumab for ATL in a tumor microenvironment-dependent animal model. Bevacizumab therapy combined with chemotherapy could be a potential treatment strategy for that subgroup of patients with ATL probably depending to a large extent on angiogenesis via VEGF for tumor survival and proliferation.

Acknowledgements

We thank Ms Chiori Fukuyama for her excellent technical assistance and Ms. Naomi Ochiai for her excellent secretarial assistance.

Funding

This study was supported by Grants-in-Aid for Scientific Research (B) (No. 25290058, T. Ishida), and Scientific Support Programs for Cancer Research (No. 221S0001, T. Ishida) from the Ministry of Education, Culture, Sports, Science and Technology of Japan, Grants-in-Aid for National Cancer Center Research and Development Fund (No. 21-6-3, T. Ishida), and H23-Third Term Comprehensive Control Research for Cancer-general-011, T. Ishida, from the Ministry of Health, Labour and Welfare, Japan.

Authorship contributions

Mori F, Ishida T, Asahi I, and Ueda R designed the research. Mori F, Ishida T, Asahi I, Sato F, Masaki A, Narita T, Suzuki S, Yamada T, and Takino H performed the research. Hishizawa M, Imada K, Takaori-Kondo A contributed to establishing the ATL mouse model. All the authors analyzed the data and wrote the article.

Conflict of interest

Nagoya City University Graduate School of Medical Sciences has received research funding for Takashi Ishida, Shigeru Kusumoto, and Shinsuke Iida from Chugai Pharmaceutical Co., Ltd. The other authors have no financial conflicts of interest related with this study.

References

1. Ishida T, Ueda R. Antibody therapy for adult T-cell leukemia-lymphoma. *Int J Hematol* 2011;**94**:443–52.
2. Matsuoka M, Jeang KT. Human T-cell leukaemia virus type 1 (HTLV-1) infectivity and cellular transformation. *Nat Rev Cancer* 2007;**7**:270–80.
3. Shimoyama M. Diagnostic criteria and classification of clinical subtypes of adult T-cell leukaemia-lymphoma. A report from the Lymphoma Study Group (1984–87). *Br J Haematol* 1991;**79**:428–37.
4. Uchiyama T, Yodoi J, Sagawa K, Takatsuki K, Uchino H. Adult T-cell leukemia: clinical and hematologic features of 16 cases. *Blood* 1977;**50**:481–92.
5. Ishida T, Hishizawa M, Kato K, *et al.* Allogeneic hematopoietic stem cell transplantation for adult T-cell leukemia-lymphoma with special emphasis on preconditioning regimen: a nationwide retrospective study. *Blood* 2012;**120**:1734–41.
6. Utsunomiya A, Miyazaki Y, Takatsuka Y, *et al.* Improved outcome of adult T cell leukemia/lymphoma with allogeneic hematopoietic stem cell transplantation. *Bone Marrow Transplant* 2001;**27**:15–20.
7. Carmeliet P, Jain RK. Molecular mechanisms and clinical applications of angiogenesis. *Nature* 2011;**473**:298–307.
8. Burger RA, Brady MF, Bookman MA, *et al.* Incorporation of bevacizumab in the primary treatment of ovarian cancer. *N Engl J Med* 2011;**365**:2473–83.
9. Escudier B, Pluzanska A, Koralewski P, *et al.* Bevacizumab plus interferon alfa-2a for treatment of metastatic renal cell carcinoma: a randomised, double-blind phase III trial. *Lancet* 2007;**370**:2103–11.
10. Escudier B, Bellmunt J, Négrier S, Bajetta E, Melichar B, Bracarda S, Ravaud A, Golding S, Jethwa S, Sneller V. Phase III trial of bevacizumab plus interferon alfa-2a in patients with metastatic renal cell carcinoma (AVOREN): final analysis of overall survival. *J Clin Oncol* 2010;**28**:2144–50.
11. Hurwitz H, Fehrenbacher L, Novotny W, *et al.* Bevacizumab plus irinotecan, fluorouracil, and leucovorin for metastatic colorectal cancer. *N Engl J Med* 2004;**350**:2335–42.
12. Perren TJ, Swart AM, Pfisterer J, *et al.* A phase 3 trial of bevacizumab in ovarian cancer. *N Engl J Med* 2011;**365**:2484–96.

13. Sandler A, Gray R, Perry MC, Brahmer J, Schiller JH, Dowlati A, Lilenbaum R, Johnson DH. Paclitaxel-carboplatin alone or with bevacizumab for non-small-cell lung cancer. *N Engl J Med* 2006;**355**:2542–50.
14. Yang JC, Haworth L, Sherry RM, Hwu P, Schwartzentruber DJ, Topalian SL, Steinberg SM, Chen HX, Rosenberg SA. A randomized trial of bevacizumab, an anti-vascular endothelial growth factor antibody, for metastatic renal cancer. *N Engl J Med* 2003;**349**:427–34.
15. Kreisl TN, Kim L, Moore K, *et al.* Phase II trial of single-agent bevacizumab followed by bevacizumab plus irinotecan at tumor progression in recurrent glioblastoma. *J Clin Oncol* 2009;**27**:740–5.
16. Bazarbachi A, Abou Merhi R, Gessain A, *et al.* Human T-cell lymphotropic virus type I-infected cells extravasate through the endothelial barrier by a local angiogenesis-like mechanism. *Cancer Res* 2004;**64**:2039–46.
17. El-Sabban ME, Merhi RA, Haidar HA, Arnulf B, Khoury H, Basbous J, Nijmeh J, de Thé H, Hermine O, Bazarbachi A. Human T-cell lymphotropic virus type 1-transformed cells induce angiogenesis and establish functional gap junctions with endothelial cells. *Blood* 2002;**99**:3383–9.
18. Hayashibara T, Yamada Y, Miyanishi T, Mori H, Joh T, Maeda T, Mori N, Maita T, Kamihira S, Tomonaga M. Vascular endothelial growth factor and cellular chemotaxis: a possible autocrine pathway in adult T-cell leukemia cell invasion. *Clin Cancer Res* 2001;**7**:2719–26.
19. Watters KM, Dean J, Gautier V, Hall WW, Sheehy N. Tax 1-independent induction of vascular endothelial growth factor in adult T-cell leukemia caused by human T-cell leukemia virus type 1. *J Virol* 2010;**84**:5222–8.
20. Ito M, Kobayashi K, Nakahata T. NOD/Shi-scid IL2rgnull (NOG) mice more appropriate for humanized mouse models. *Curr Top Microbiol Immunol* 2008;**324**:53–76.
21. Abramoff MD, Magelhaes PJ, Ram SJ. Image Processing with ImageJ. *Biophotonics Int* 2004;**11**:36–42.
22. Imada K, Takaori-Kondo A, Sawada H, Imura A, Kawamata S, Okuma M, Uchiyama T. Serial transplantation of adult T cell leukemia cells into severe combined immunodeficient mice. *Jpn J Cancer Res* 1996;**87**:887–92.
23. Suzuki S, Masaki A, Ishida T, *et al.* Tax is a potential molecular target for immunotherapy of adult T-cell leukemia/lymphoma. *Cancer Sci* 2012;**103**:1764–73.
24. Mori F, Ishida T, Ito A, *et al.* Potent antitumor effects of bevacizumab in a microenvironment-dependent human lymphoma mouse model. *Blood Cancer J* 2012;**2**:e67.
25. Mohammad RM, Wall NR, Dutcher JA, Al-Katib AM. The addition of bryostatin 1 to cyclophosphamide, doxorubicin, vincristine, and prednisone (CHOP) chemotherapy improves response in a CHOP-resistant human diffuse large cell lymphoma xenograft model. *Clin Cancer Res* 2000;**6**:4950–6.
26. Motoi T, Uchiyama T, Uchino H, Ueda R, Araki K. Serum soluble interleukin-2 receptor levels in patients with adult T-cell leukemia and human T-cell leukemia/lymphoma virus type-I seropositive healthy carriers. *Jpn J Cancer Res* 1988;**79**:593–9.
27. Ito A, Ishida T, Utsunomiya A, *et al.* Defucosylated anti-CCR4 monoclonal antibody exerts potent ADCC against primary ATLL cells mediated by autologous human immune cells in NOD/Shi-scid, IL-2R gamma(null) mice *in vivo*. *J Immunol* 2009;**183**:4782–91.
28. Masaki A, Ishida T, Suzuki S, *et al.* Autologous Tax-Specific CTL therapy in a primary adult T cell leukemia/lymphoma cell-bearing NOD/Shi-scid, IL-2Rγnull mouse model. *J Immunol* 2013;**191**:135–44.
29. Wang ES, Teruya-Feldstein J, Wu Y, Zhu Z, Hicklin DJ, Moore MA. Targeting autocrine and paracrine VEGF receptor pathways inhibits human lymphoma xenografts *in vivo*. *Blood* 2004;**104**:2893–902.
30. Koga H, Imada K, Ueda M, Hishizawa M, Uchiyama T. Identification of differentially expressed molecules in adult T-cell leukemia cells proliferating *in vivo*. *Cancer Sci* 2004;**95**:411–7.
31. Yu L, Wu X, Cheng Z, Lee CV, LeCouter J, Campa C, Fuh G, Lowman H, Ferrara N. Interaction between bevacizumab and murine VEGF-A: a reassessment. *Invest Ophthalmol Vis Sci* 2008;**49**:522–7.
32. Ellis LM, Hicklin DJ. VEGF-targeted therapy: mechanisms of anti-tumour activity. *Nat Rev Cancer* 2008;**8**:579–91.
33. Carmeliet P, Jain RK. Principles and mechanisms of vessel normalization for cancer and other angiogenic diseases. *Nat Rev Drug Discov* 2011;**10**:417–27.
34. Jain RK. Normalization of tumor vasculature: an emerging concept in antiangiogenic therapy. *Science* 2005;**307**:58–62.
35. Maemondo M, Inoue A, Kobayashi K, *et al.* Gefitinib or chemotherapy for non-small-cell lung cancer with mutated EGFR. *N Engl J Med* 2010;**362**:2380–8.
36. Bardelli A, Siena S. Molecular mechanisms of resistance to cetuximab and panitumumab in colorectal cancer. *J Clin Oncol* 2010;**28**:1254–61.
37. Lambrechts D, Lenz HJ, de Haas S, Carmeliet P, Scherer SJ. Markers of response for the antiangiogenic agent bevacizumab. *J Clin Oncol* 2013;**31**:1219–30.
38. Ishida T, Joh T, Uike N, *et al.* Defucosylated anti-CCR4 monoclonal antibody (KW-0761) for relapsed adult T-cell leukemia-lymphoma: a multicenter phase II study. *J Clin Oncol* 2012;**30**:837–42.
39. Tanosaki R, Tobinai K. Adult T-cell leukemia-lymphoma: current treatment strategies and novel immunological approaches. *Expert Rev Hematol* 2010;**3**:743–53.
40. Marçais A, Suarez F, Sibon D, Frenzel L, Hermine O, Bazarbachi A. Therapeutic options for adult T-cell leukemia/lymphoma. *Curr Oncol Rep* 2013;**15**:457–64.